

Layer-by-layer phase transformation in Ti_3O_5 revealed by machine learning molecular dynamics simulations

Mingfeng Liu,^{1,2,*} Jiantao Wang,^{1,2,*} Junwei Hu,^{3,*} Peitao Liu,^{1,†} Haiyang Niu,^{3,†} Xuexi Yan,¹ Jiangxu Li,¹ Haile Yan,⁴ Bo Yang,⁴ Yan Sun,¹ Chunlin Chen,¹ Georg Kresse,⁵ Liang Zuo,⁴, and Xing-Qiu Chen¹

¹ Shenyang National Laboratory for Materials Sciences, Institute of Metal Research, Chinese Academy of Sciences, Shenyang 110016, China

² School of Materials Science and Engineering, University of Science and Technology of China, Shenyang 110016, China

³ State Key Laboratory of Solidification Processing, International Center for Materials Discovery, School of Materials Science and Engineering, Northwestern Polytechnical University, Xi'an 710072, China

⁴ Key Laboratory for Anisotropy and Texture of Materials (Ministry of Education), School of Materials Science and Engineering, Northeastern University, Shenyang 110819, China

⁵ University of Vienna, Faculty of Physics, Computational Materials Physics, Kolingasse 14-16, 1090 Vienna, Austria

† Corresponding to: ptliu@imr.ac.cn, haiyang.niu@nwpu.edu.cn

* These authors contribute equally.

Abstract

Reconstructive phase transitions involving breaking and reconstruction of primary chemical bonds are ubiquitous and important for many technological applications. In contrast to displacive phase transitions, the dynamics of reconstructive phase transitions are usually slow due to the large energy barrier. Nevertheless, the reconstructive phase transformation from β - to λ - Ti_3O_5 exhibits an ultrafast and reversible behavior. Despite extensive studies, the underlying microscopic mechanism remains unclear. Here, we discover a kinetically favorable in-plane nucleated layer-by-layer transformation mechanism through metadynamics and large-scale molecular dynamics simulations. This is enabled by developing an efficient machine learning potential with near first-principles accuracy through an on-the-fly active learning method and an advanced sampling technique. Our results reveal that the β - λ phase transformation initiates with the formation of two-dimensional nuclei in the ab -plane and then proceeds layer-by-layer through a multistep barrier-lowering kinetic process via intermediate metastable phases. Our work not only provides important insight into the ultrafast and reversible nature of the β - λ transition, but also presents useful strategies and methods for tackling other complex structural phase transitions.

arXiv:2310.05683v2 [cond-mat.mtrl-sci] 3 Apr 2024

Introduction

Solid-solid phase transitions are arguably one of the most ubiquitous phenomena in nature and have important implications for numerous scientific areas such as metallurgy [1], ceramics [2, 3], diamond production [4, 5], earth sciences [6, 7], and so on. Typically, the solid-solid phase transitions can be categorized into two main classes. One is the displacive (martensitic) type where the atomic configuration evolves with short-range shifts of atoms and no chemical bonds are broken. The other one is the reconstructive type which involves breaking and reconstruction of part of the chemical bonds and exhibits drastic changes at the transition point with large latent heat and thermal hysteresis [8]. In contrast to the displacive phase transitions, the dynamics of the reconstructive phase transitions are usually slow because of the need to overcome a large free-energy barrier [9–12]. This raises an important question of whether it is possible to obtain ultrafast dynamics in a reconstructive phase transition, which is highly desirable for designing novel functional devices with fast response to external stimuli. Interestingly, the isostructural phase reconstruction from the low-temperature semiconducting β - Ti_3O_5 phase to the high-temperature metallic λ - Ti_3O_5 phase observed in recent experiments is one representative example meeting such a condition [13–17]. The transition is of first order with a large latent heat and exhibits abnormal ultrafast and reversible characteristics [13–17]. The reversibility can be achieved by applying pressure and heat, pressure and light, or pressure and current [13–15]. These unique structural and functional properties of Ti_3O_5 therefore have stimulated extensive research interests towards technological applications in optical storage media [13], energy storage [13–15, 18–20], solar steam generation [21], and gas sensors [22–24].

To understand the nature of the phase transformation between the β and λ phases, many studies have been carried out. It was argued that the phase transition is driven by the coupling between the crystal lattice and excited electrons (or holes) [25] or induced by tensile strain [26]. Recent ultrafast powder X-ray diffraction (XRD) measurements, however, demonstrated that the strain waves propagating in a timescale of several picoseconds govern the phase transition [16]. Due to the anisotropy of the strain associated with the phase transition, the photoinduced phase transition in a single crystal of Ti_3O_5 occurs only when the pump pulse is applied on the *ab* plane [17]. This process has been recently resolved by direction-dependent interface propagation using interface models optimized by machine learned force field method [27]. A recent study on doping reveals that it primarily alters the relative energy of both phases, but not the activation barrier [28]. Despite extensive studies, the underlying transition mechanism at an atomic level, particularly the kinetic pathway for the ultrafast and reversible transition, remains unclear. This is a known challenging task for both experimental measurements and theoretical modeling. Specifically, experimental measurements often lack sufficient spatial and temporal resolution to capture atomistic events, whereas theoretical modeling requires accurate sampling of the potential energy surface (PES). *Ab initio* molecular dynamics (AIMD), albeit with high accuracy, struggle in terms of the accessible time and length scales. Although machine learning potentials (MLPs) [29–40] can significantly speed up MD simulations while retaining first-principles accuracy, exploring the time scales over which the β - λ phase transition occurs still represents a challenge. By contrast, advanced sampling techniques such as metadynamics [41–43] allow for efficient sampling of the PES of interest, and therefore have been successfully used to study barrier-crossing rare events [10–12, 44–49].

In this work, we have developed an accurate and efficient MLP through a combined on-the-fly active learning and advanced sampling method. It allows us to perform metadynamics simulations and large-scale MD simulations with *ab initio* accuracy and discover a kinetically favorable microscopic mechanism for the reconstructive β - λ phase transition. Our results unveil that the phase transition undergoes an interesting in-plane nucleated layer-by-layer kinetic transformation pathway. This is manifested by favorable in-plane intra-cell atomic movements forming two-dimensional (2D) nuclei, followed by propagating to neighboring layers via intermediate metastable crystalline phases comprised of β -like and λ -like structural motifs when the lattice strain along the *c* axis increases. Interestingly, we find that superlattices consisting of any combination of β -like and λ -like building blocks along the *c* axis are all metastable phases with no imaginary phonon modes. The presence of intermediate layer-by-layer kinetic transformation pathways greatly reduces the free-energy barrier, thereby naturally explaining why an ultrafast and reversible phenomenon can appear in a reconstructive solid-solid phase transition.

Results

Machine learning potential development

Let us start with the MLP construction and validation. To develop an accurate MLP for describing the β - λ phase transition, a representative training dataset covering the phase space of interest is indispensable. This was achieved by combining an on-the-fly active learning procedure and the enhanced sampling technique (see "Methods"). The final training dataset consists of 3,775 structures of 96 atoms, on which the MLP was generated using a moment tensor potential [50]. Through the kernel principal component analysis [51] using the smooth overlap of atomic position descriptors [52], we found that the training structures are indeed very representative and cover a wide range of the phase space. In particular, the phase transition pathway is well sampled by metadynamics simulations (Supplementary Fig. 1a). The generated MLP was carefully validated on a test dataset including 748 structures of 96 atoms and it is capable to accurately predict the lattice parameters, energy-volume curves, and phonon dispersion relations of both β - and λ - Ti_3O_5 , all in good agreement with the underlying density functional theory (DFT) calculations as well as available experimental data (Supplementary Table 1, Supplementary Fig. 1b-c and Supplementary Fig. 2). For more details on the MLP construction and validation, we refer to "Methods". It is worth mentioning that the present MLP is also able to describe well the high-temperature α - Ti_3O_5 phase (Supplementary Table 1 and Supplementary Fig. 1b-c). In particular, the presence of imaginary phonon modes at 0 K and the absence of imaginary phonon modes at high temperatures due to anharmonic phonon-phonon interactions have been well reproduced by our developed MLP (Supplementary Fig. 1). This is not unexpected, since α - Ti_3O_5 shares similar local structural motifs as λ - Ti_3O_5 .

Kinetically favorable layer-by-layer transformation pathway

Both the β - and λ - Ti_3O_5 phases have a monoclinic structure with the same space group of $C2/m$ (Fig. 1d). In addition, their lattice parameters are very close, with the λ phase exhibiting a slightly larger *c* lattice constant (Supplementary Table 1). The noticeable difference between the two phases lies in that they exhibit distinct local structural motifs around the Ti3-Ti3 dimers, whereas the local structural environments around Ti1 and Ti2 atoms are similar. The phonon mode analysis indicates that the A_g phonon mode at Γ with 3.72

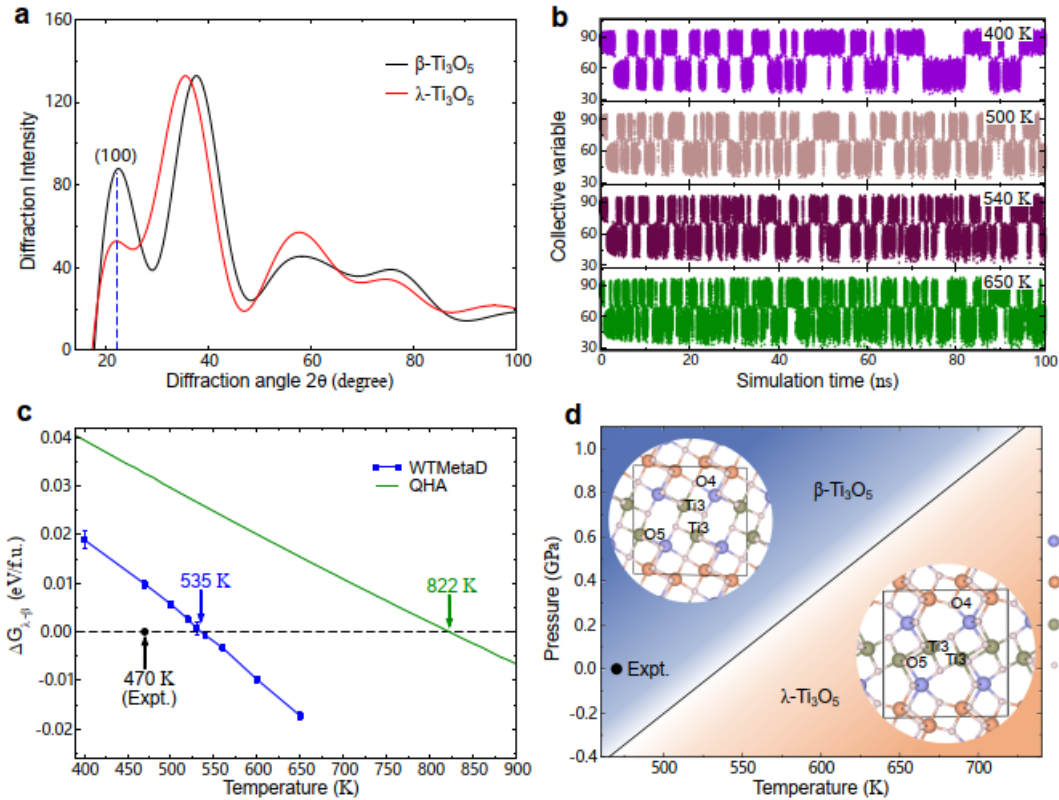


Fig. 1 | Metadynamics simulations and phase diagram. **a**, Simulated XRDs of β - and λ - Ti_3O_5 using a 96-atom supercell. **b**, Time evolution of collective variable at different temperatures and 0 GPa. **c**, Free energy difference $\Delta G_{\lambda-\beta}$ calculated by the well-tempered variant of metadynamics (WTMetaD) and the quasi-harmonic approximation (QHA) as a function of temperature. The energy is given in electron volt per formula unit (eV/f.u.). The error bar indicates the standard deviation from three independent simulations. The predicted and experimental phase transition temperatures are indicated by arrows. **d**, Pressure-temperature phase diagram predicted by metadynamics simulations. Insets show the crystal structures of β - and λ - Ti_3O_5 , where the black lines indicate the unit cell. The experimental data (denoted as Expt.) in **c** and **d** are taken from ref. [14]. Source data are provided as a Source Data file. The structure models used are provided in Supplementary Data.

THz is responsible for the transition from β to λ , as the mode softens as the temperature increases. Reversibly, when going from λ to β , the A_g phonon mode at Γ with 4.58 THz plays a dominant role. It becomes soft as the pressure is increased over 3 GPa (see Supplementary Fig. 3). We note that the B_u mode at Γ previously identified in ref. [14] is not the decisive phonon mode to derive the phase transformation, since by following the eigenvector of this mode one can not obtain the transition state with the typical feature of the rotation of Ti3-Ti3 dimers. Our phonon mode analysis are in line with our metadynamics simulations (see "Methods"), which show that during the β to λ transition the Ti3-Ti3 dimers undergo a gradual rotation, accompanied by the breaking of Ti3-O4 bond and the formation of Ti3-O5 bond (Supplementary Fig. 4). It is interesting to note that only the atoms involving the Ti3-Ti3 dimers and associated O atoms participate in the intra-cell atomic movements, while the other atomic layers including Ti1 and Ti2 atoms almost remain unchanged. Our observations corroborate the structural changes inferred by femtosecond powder XRD [16].

On the thermodynamic side, we computed Gibbs free energy via metadynamics simulations. For the choice of collective variable (CV), following ref. [46] the intensity of the XRD peak at $2\theta = 22^\circ$ [corresponding to the (100) plane] was used (Fig. 1a). It turns out that the employed CV is very efficient and can effectively distinguish the two phases, as manifested by frequent reversible transitions between the two phases (Fig. 1b). Using the reweighting technique [53], the Gibbs free energies of the two phases were computed. By fully accounting for the anharmonic effects, the calculated phase

transition temperature T_c and phase transition enthalpy ΔH at 0 GPa are 535 K and 0.091 eV/f.u., respectively, in good agreement with the experimental values ($T_c=470$ K and $\Delta H=0.124\pm 0.01$ eV/f.u.) [14] (Fig. 1c). By contrast, the quasi-harmonic approximation significantly overestimates the transition temperature (Fig. 1c). Using a similar procedure, a full *ab initio* pressure-temperature phase diagram has been established (Fig. 1d).

Kinetically, the direct phase transformation from β to λ in a concerted manner needs to overcome a larger energy barrier of 0.25 eV/f.u., as revealed by our variable-cell climbing image nudged elastic band (CI-NEB) calculations at 0 K (see Supplementary Fig. 5 and also ref. [54]). This seems incompatible with the experimentally observed ultrafast and reversible nature of the transition [14, 16], indicating that the phase transition must undergo intermediate barrier-lowering kinetic transformation pathways. To confirm this, we computed the PES through metadynamics simulations using a supercell including three Ti3-Ti3 layers (Fig. 2a). The CVs were designed to be able to well describe the degree of the rotations of Ti3-Ti3 dimers in each layer (see "Methods" and Supplementary Fig. 6a). The computed free energy surface at 600 K and 0 GPa as a function of the employed CVs indeed identifies four energy minima, which correspond to β - Ti_3O_5 , a $\beta\beta\lambda$ -stacking phase, a $\beta\lambda\lambda$ -stacking phase, and λ - Ti_3O_5 , respectively (Fig. 2b). Our phonon calculations revealed that both the $\beta\beta\lambda$ -stacking and $\beta\lambda\lambda$ -stacking phases are dynamically stable (Supplementary Fig. 8). More interestingly, we predicted that all superlattices consisting of any combination of β -like and λ -like structural motifs along the c direction are dynami-

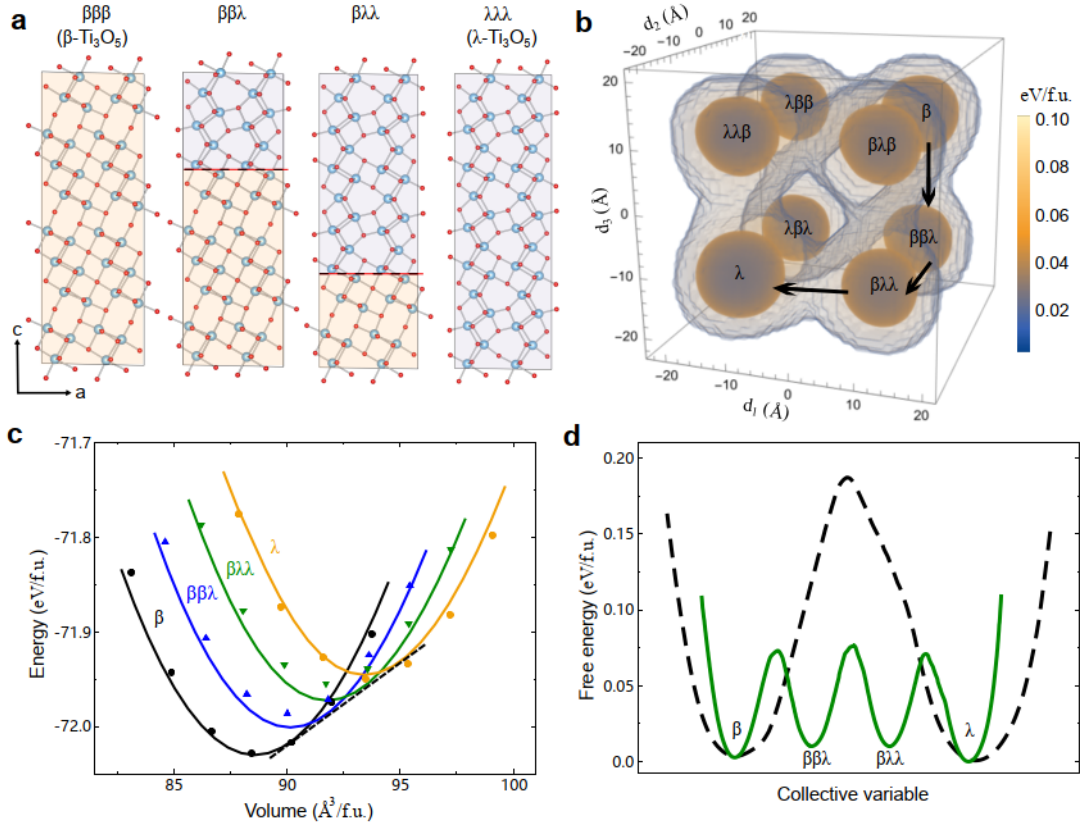


Fig. 2 | Predicted metastable phases and their potential energy surface. **a**, Structures of β - Ti_3O_5 , $\beta\beta\lambda$ -stacking metastable phase, $\beta\lambda\lambda$ -stacking metastable phase and λ - Ti_3O_5 , respectively. The light yellow and purple colors represent the β -like and λ -like structural motifs, respectively. The blue and red balls represent Ti and O atoms, respectively. **b**, Free energy surface (in electron volt per formula unit, i.e., eV/f.u.) computed from metadynamics simulations at 600 K and 0 GPa. For definition of collective variables d_i ($i=1, 2$ and 3), we refer to "Methods" and Supplementary Fig. 6a. Note that $\beta\beta\lambda$, $\lambda\beta\beta$, and $\beta\lambda\beta$ are symmetry-equivalent structures, and similarly, $\beta\lambda\lambda$, $\lambda\beta\lambda$, and $\lambda\lambda\beta$ are symmetry-equivalent structures. **c**, Energy-volume curves predicted by DFT (circles and triangles) and machine learning potential (solid lines) at 0 K and 0 GPa. **d**, Potential energy surface (PES) obtained at 600 K and 0 GPa as a function of employed collective variable. The black dashed line denotes the PES for a concerted β - λ phase transition, whereas the green solid lines denote the PES for the transition pathway through intermediate metastable phases (corresponding to arrows in **b**). Source data are provided as a Source Data file. The structure models used are provided in Supplementary Data.

cally stable (Supplementary Fig. 7 and Supplementary Fig. 8). They all adopt the same space group of $C2/m$. The dynamical stabilities were confirmed by performing phonon calculations on superlattices with up to eight building blocks using the developed MLP. The MLP predictions were verified by DFT calculations on small superlattices such as two-layer-stacking $\beta\lambda$ phase and three-layer-stacking $\beta\beta\lambda$ and $\beta\lambda\lambda$ phases (Supplementary Fig. 8a-c).

We further computed the energy-volume curves at 0 K and 0 GPa (Fig. 2c). One can see that the system volume (mostly the c lattice constant) increases as the number of λ -like building blocks increases. The energy-volume curves of the metastable $\beta\beta\lambda$ and $\beta\lambda\lambda$ phases are evenly located between the ones of β - Ti_3O_5 and λ - Ti_3O_5 . They almost share a common tangent line, implying that under a specific negative pressure the β to λ phase transformation is likely to go through the intermediate $\beta\beta\lambda$ and $\beta\lambda\lambda$ metastable phases. Indeed, the free energies computed by metadynamics simulations at 600 K and 0 GPa demonstrated that as compared to the concerted β - λ phase transition, the existence of the intermediate $\beta\beta\lambda$ and $\beta\lambda\lambda$ metastable phases significantly reduces the energy barrier from 0.19 eV/f.u. to 0.07 eV/f.u. (Fig. 2d), a small value for a solid-solid phase transition. The metadynamics free energy calculations are in line with the variable-cell CI-NEB calculations using the same three-layer supercell (Supplementary Fig. 9a). We would like to stress that the obtained layer-by-layer kinetic transformation mechanism is not limited to the three-layer supercell. Similar observations were also

obtained for a larger five-layer supercell (Supplementary Fig. 9b). We note that this is the so-called Ostwald's "rule of stages" [55], which has been experimentally proved in solid-solid transitions of colloidal crystals mediated by a transient liquid intermediate [56]. However, the finding of metastable crystalline phases serving as the intermediate for a reconstructive solid-solid phase transition is rare.

The discovered kinetically favorable layer-by-layer transformation pathway is essentially determined by the specific structure correlation between the two phases. The shared common structural features (i.e., non-displacive Ti1-Ti1 and Ti2-Ti2 layers) exhibit twofold effects. One is to connect the β - or λ -like structural building blocks resulting in Lego-like metastable phases, and the other is to serve as blocking layers for the inter-layer propagation leading to the layer-by-layer kinetic transformation pathway. During the β - λ phase reconstruction, only Ti and O atoms associated with the Ti3-Ti3 layers are involved. In addition, only the relatively weak Ti3-O4 and Ti3-O5 chemical bonds need to be broken for $\beta \rightarrow \lambda$ and $\lambda \rightarrow \beta$, respectively. This is evidenced by the DFT calculated electron localization functions (Supplementary Fig. 10) and also by the chemical analysis using integrated crystal-orbital Hamiltonian populations by Fu *et al.* [25]. In contrast, the Ti3-Ti3 chemical bonds forming a σ -bonding of d_{xy} -like states [21] remain intact. This explains why the value of the energy barrier for the β - λ transformation is low. Our observation provides a natural explanation for the ultrafast and reversible nature of the β - λ transition [14, 16].

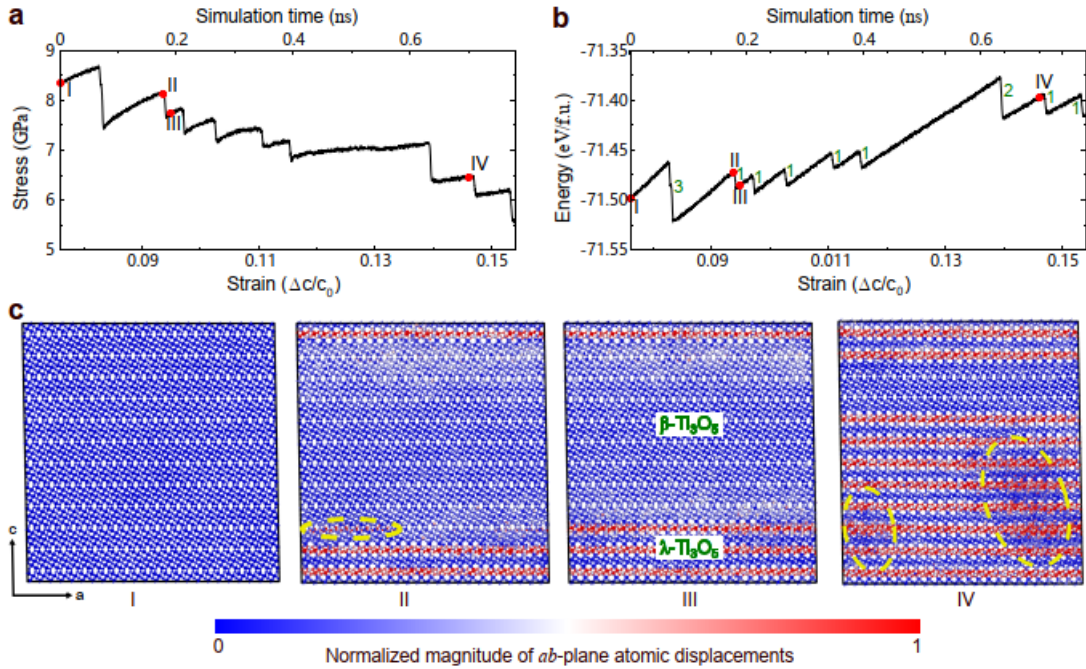


Fig. 3 | Direct MD simulations under tensile strain at 300 K and 0 GPa using a large cell including 165,888 atoms. **a-b**, Evolution of stress and potential energy (in electron volt per formula unit, i.e., eV/f.u.) with respect to strain under c -axis unidirectional continuous tensile strain (strain rate 10^8 /s). The values close to each jump of the potential energy in **b** indicate the number of layers undergoing the β to λ transition. **c**, Snapshots at the simulation times indicated by red dots in **a-b**. The Ti and O atoms are denoted by large and small balls, respectively. The yellow dashed circle in snapshot II highlights the 2D nucleation in the ab -plane, while the two yellow dashed circles in snapshot IV mark the defective regions. Source data are provided as a Source Data file. The configurations presented are provided in Supplementary Data.

Evidence of in-plane nucleated multistep kinetic mechanism

To further corroborate the layer-by-layer multistep kinetic mechanism for the β - λ phase transition as revealed by metadynamics simulations, we performed unbiased direct MD simulations. However, our tests showed that direct MD simulations were not capable of overcoming the energy barrier for the β - λ phase transition on a nanosecond timescale. Nevertheless, applying unidirectional tensile strain along the c -axis can significantly reduce the energy barrier (see Supplementary Fig. 11), making direct MD simulations possible [26]. Indeed, with a unidirectional tensile strain in the c -direction, the first-order phase transition from β to λ was successfully reproduced within ~ 1 ns by direct MD simulations on a 96-atom cell using the MLP, as manifested by an abrupt jump in the potential energy as well as stress (see Supplementary Fig. 12a-b). A closer inspection of local structure changes from the direct MD simulations verifies the metadynamics results (compare Supplementary Fig. 12c to Supplementary Fig. 4). We note in passing that applying a c -axis unidirectional strain in DFT also drives the β - λ phase transition (Supplementary Fig. 13).

In order to exclude the size effects and further clarify the phase transition details, we carried out large-scale MD simulations under continuously increasing tensile strain along the c axis using a large cell with 165,888 atoms (see "Methods" for details). Structural evolutions similarly to the small cell discussed above were observed (compare Fig. 3 to Supplementary Fig. 12). Nevertheless, the 2D in-plane nucleation and growth behavior accompanied by step-wise changes in the potential energy and stress can be better visualized in the large-scale MD simulations (see Fig. 3 and Supplementary Movie 1). It is interesting to observe that under continuously increasing tensile strain the β phase does not transform to the λ phase simultaneously in one step, but rather the transformation starts by the formation of a 2D nuclei in the ab -plane and then grows succes-

sively layer-by-layer along the c axis mediated by metastable phases (see Fig. 3c). The easy propagation along the c axis arises from the lower energy barrier as compared to other two (a and b) directions, as recently revealed by Jütten and Bredow [27]. The deformation involving the Ti3-Ti3 dimers and associated O atoms does not propagate to the neighboring layers until the present layer completes the transition to the λ -Ti₃O₅-like structural motifs. The characteristic 2D growth behavior of the β - to λ -Ti₃O₅ transition is reflected by the step-wise potential energy as a function of strain (Fig. 3b). The growth of the λ -like structural motifs causes the tensile strain for the neighboring layers. This would decrease the kinetic energy barrier (Supplementary Fig. 11), thereby facilitating the layer-by-layer β to λ transformation. We note that the 2D layer-by-layer growth behavior can be better captured by using a smaller strain rate (Supplementary Fig. 14). In line with previous metadynamics results, our large-scale unbiased MD simulations consolidate the in-plane nucleated layer-by-layer kinetic mechanism for the β to λ transition and corroborate the strain wave pathway derived by experiment [16]. We notice that during the β to λ transition in the large-scale MD simulations, a defective metastable phase featured by incomplete rotation of Ti3-Ti3 dimers appears (Fig. 3c and Supplementary Fig. 15). This is likely caused by anisotropic strain energies associated with inhomogeneous lattice distortions [17], because this metastable phase is found to be stable only under tensile strain and will transform to the more stable β phase after full structural relaxation.

It should be noted that the 2D in-plane nucleation and growth behavior of the β - λ phase transition is robust, regardless of the presence of external tensile strain. To demonstrate this, we carried out a computational experiment by artificially embedding a λ -Ti₃O₅-like nucleus with a radius of 60 Å in the β -Ti₃O₅ matrix (see "Methods" for details). The employed supercell model including 122,880 atoms is shown in Fig. 4a-b. This allows us to overcome the energy bar-

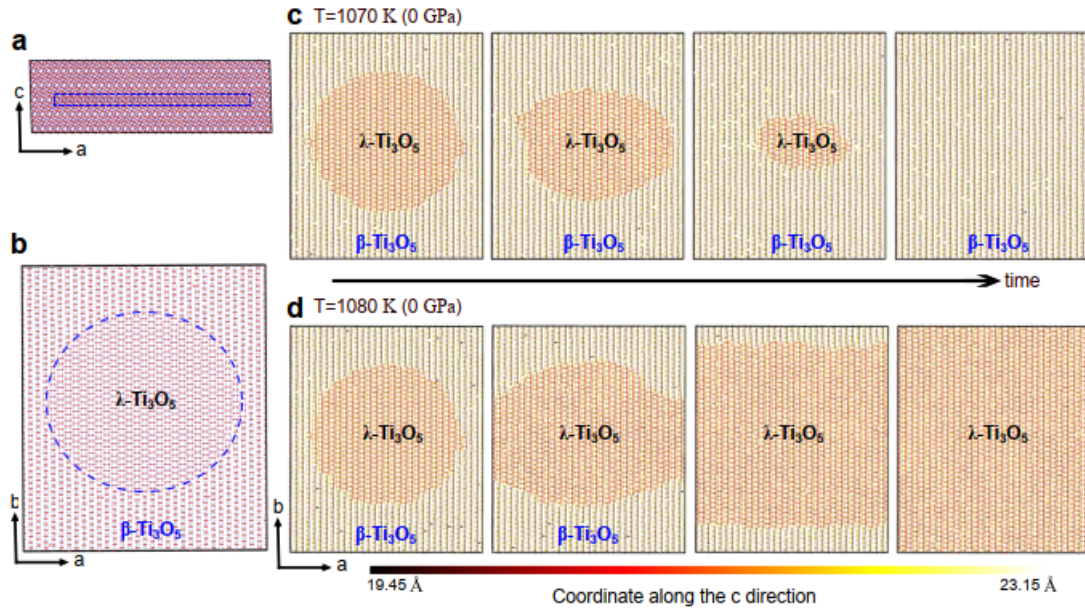


Fig. 4 | Large-scale 2D phase growth MD simulations. **a-b**, Side and top views of employed structural model consisting of 122,880 atoms. A λ - Ti_3O_5 -like nucleus with a thickness equal to the c -axis lattice constant was artificially created in a region with a radius of 60 Å (marked by dashed lines) in the middle of the β - Ti_3O_5 matrix. The large and small spheres represent the Ti and O atoms, respectively. **c**, Snapshots from an MD simulation at 1070 K and 0 GPa. **d**, Snapshots from an MD simulation at 1080 K and 0 GPa. Note that in **b-d** only the layer containing the λ - Ti_3O_5 -like nucleus is shown. The initial and final configurations are provided in Supplementary Data.

rier of the β to λ transition and study the propagation and annihilation processes of the λ - Ti_3O_5 -like nucleus by just tuning the temperature and pressure in a direct isothermal-isobaric MD simulation without applying any external forces. We found that at ambient pressure the preexisting λ - Ti_3O_5 -like nucleus grows only within the layer and eventually extends to the full layer as the temperature goes over 1080 K. Below 1080 K it gradually disappears (see Fig. 4c-d and Supplementary Movie 2). However, the inter-layer propagation did not take place, in contrast to the tensile MD simulations. This is due to the insufficient driving force along the c axis. We note that the temperature at which the preexisting λ - Ti_3O_5 -like nucleus starts to grow is higher than the thermodynamic phase transition temperature. This is likely caused by the presence of compressive strain in the nucleus. Indeed, the critical transition temperature is decreased when reducing the pressure to a negative value, and vice versa (Supplementary Fig. 16), in accordance with the established pressure-temperature phase diagram (Fig. 1). Our computational experiments combined with the c -axis tensile MD simulations clearly demonstrate that the intra-layer transformation and growth are more favorable, whereas the inter-layer growth starts to occur only when the c -axis strain is sufficiently large.

Kinetics of in-plane nucleation and growth

As discussed above, the β - λ phase transformation is initiated through in-plane nucleation and subsequently expands in a layer-by-layer manner. Nevertheless, further investigation is required to understand the specific kinetics involved in the process of in-plane nucleation and growth. To this end, we carried out variable-cell CI-NEB calculations using the MLP for transforming one layer of β - Ti_3O_5 from β -like to λ -like structural motifs. The results are displayed in Fig. 5. It is clear that the direct transformation in a concerted manner is energetically unfavorable because of the need to overcome a relatively large energy barrier (0.09 eV/f.u.) (see Path I in Fig. 5b). By contrast, the transformation via the in-plane nucleation is kinetically more favorable, with a decreased energy barrier

of 0.07 eV/f.u. for the employed specific supercell (see Path II in Fig. 5b). We note that for the case of the nucleation mechanism, the energy barrier B is independent of the system size N , resulting in $B/N \sim 0$ when N is large, while for the case of a collective mechanism, the energy barrier B increases linearly with the system size N , leading to a constant ratio B/N with respect to N (see Supplementary Fig. 18). Furthermore, one can see that once the nucleation occurs, the subsequent in-plane growth proceeds with ease. Intriguingly, the in-plane growth process unveiled the presence of further intermediate metastable phases (B2 and B4 in Fig. 5b), whose dynamical stabilities were confirmed by phonon calculations (see Supplementary Fig. 17). The transformation from the metastable phase B2 to the metastable phase B4 only needs to overcome a minute energy barrier of 6 meV/f.u. (see Fig. 5b), indicating the easy in-plane growth. More detailed transformations for Paths I and II are provided in Supplementary Movie 3.

Discussion

Accurate atomistic simulations of solid-solid structural phase transitions are challenging. Simulations are hindered by the slow dynamics and the lack of accurate and efficient interatomic potentials. Here, the issue has been addressed by developing an efficient MLP with near first-principles accuracy through a combination of an on-the-fly active learning method and an advanced sampling technique. It is remarkable that the generated MLP based on a simple standard PBE functional is capable to simultaneously describe well the lattice parameters, energy-volume curves, phase transition temperature and phonon dispersion relations of both the β - and λ - Ti_3O_5 phases, and the high-temperature α - Ti_3O_5 phase. It also predicts Lego-like metastable phases that are not included in the training dataset. It is noteworthy that the PBE functional incorrectly predicts β - Ti_3O_5 to be a metal. PBEsol, SCAN and hybrid functionals are also unable to open a band gap in β - Ti_3O_5 if magnetic ordering is not considered. Our study indicates that the electron correlation effects may not play a decisive role for the β - λ structural phase transition.

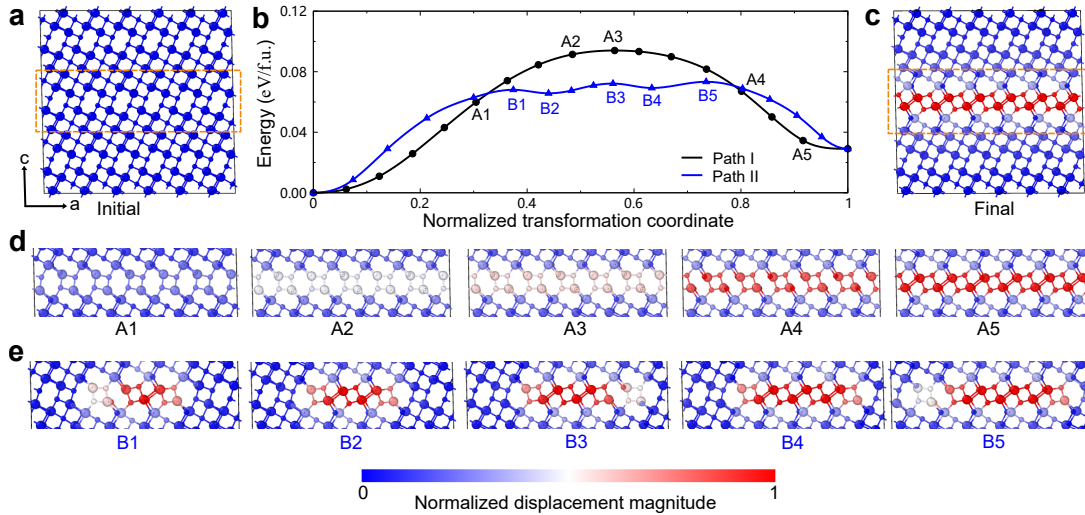


Fig. 5 | Variable-cell climbing image nudged elastic band calculations for transforming one layer of β - Ti_3O_5 from β -like to λ -like structural motifs. **a**, Employed initial structure of β - Ti_3O_5 including 288 atoms. **b**, Computed relative energies (in electron volt per formula unit, i.e., eV/f.u.) as a function of normalized transformation coordinate for two pathways. Path I denotes that the transformation proceeds in a concerted manner, whereas Path II indicates that the transformation initiates from nucleation and then proceeds via intermediate phases. **c**, Final structure of the transformation. **d**, Selected structures along the Path I. **e**, Selected structures along the Path II. Note that for a better presentation, only the atoms inside the dashed rectangle in **a** are shown and the atoms are color-coded according to the magnitude of displacements relative to the initial β - Ti_3O_5 phase. The large and small balls represent the Ti and O atoms, respectively. Source data are provided as a Source Data file. The structure models used are provided in Supplementary Data.

Fundamentally, the implications of the present study are intriguing as it suggests that the phase transitions in Ti_3O_5 can be described on the level of the simplest mean field theory neglecting magnetism. It might be worthwhile to study the influence of vibrational contributions on phase transitions in other materials that are broadly considered to be strongly correlated. We note in passing that very recently an MLP was also developed by Jütten and Bredow [27] to study the pressure effect on the phase transition of Ti_3O_5 . However, their developed MLP was mainly used to optimize the interface models with mixed phases, while the kinetic phase transition details have not been explored.

The carefully validated MLP not only allows us to perform metadynamics simulations, but also enables to carry out large-scale MD simulations. Using the intensity of the XRD peak as a collective variable for the metadynamics simulations, a full *ab initio* thermodynamic pressure-temperature phase diagram for the β and λ phases has been constructed, in good agreement with experiments. By performing large-scale MD simulations under *c*-axis unidirectional tensile strain and using computational experiments with a preexisting λ -like nucleus in a β matrix, we have clarified that the phase transformation starts with favorable 2D nucleation in the *ab*-plane, and then propagates to the neighboring layers through a multi-step barrier-lowering kinetic pathway via intermediate metastable crystalline phases. This kinetically favorable in-plane nucleated multistep mechanism has not been revealed before and provides a straightforward interpretation of the experimentally observed unusual ultrafast dynamics in the reconstructive β - λ transition. Due to the structural similarity, we expect that the microscopic transition mechanism obtained here should also apply to phase transitions of other titanium suboxides, e.g., the γ - to δ - Ti_3O_5 transition [57] and phase transitions in Ti_4O_7 [58].

Finally, we would like to emphasize that the observed metastable phases are particularly interesting, since periodic superlattices formed by any combination of β -like and λ -like building blocks along the *c* axis are all dynamically stable. This flexibility opens avenues for tuning functional properties, e.g., insulator-to-metal

transition and specific heat modulation. Consequently, our findings hold great potential for practical applications in the design of novel energy storage media, optical storage media and sensor devices. Moreover, given the success of the developed MLP in predicting many undiscovered metastable phases, combining the present MLP with structure search tools would allow us to efficiently explore more unknown stable/metastable phases not just limited to a small number of atoms [59]. Our work not only gives important insight into the microscopic mechanism for the β - λ phase transition, but also provides useful strategies and methods that can be widely used to tackle other complex structural phase transitions.

Methods

First-principles calculations

The first-principles calculations were performed using the Vienna *ab initio* simulation package (VASP) [60]. The generalized gradient approximation of Perdew-Burke-Ernzerhof (PBE) [61] was used for the exchange-correlation functional, which yields an excellent description of the experimental lattice parameters of both β - and λ - Ti_3O_5 as compared to other density functionals such as PBEsol [62] and SCAN [63] (see Supplementary Table 1). The standard projector-augmented-wave potentials ($\text{Ti}_{i_{sv}}$ and O) were used. A plane wave cutoff of 520 eV and a Γ -centered *k*-point grid with a spacing of 0.21 \AA^{-1} between *k* points (corresponding to a $3 \times 3 \times 3$ *k*-point grid for a 96-atom supercell) were employed. This ensures that the total energy is converged to better than 1 meV/atom. The Gaussian smearing method with a smearing width of 0.05 eV was used. Whenever ground state structures were required, the electronic optimization was performed until the total energy difference between two iterations was less than 10^{-6} eV. The structures were optimized until the forces were smaller than 1 meV/\AA . Since it was experimentally found that the β phase is a nonmagnetic semiconductor, while the λ phase is a weak Pauli paramagnetic metal [13, 64], nonmagnetic setups were thus adopted for all the calculations. This is a reasonable choice, since adopting the PBE functional with non-

magnetic setups yields good descriptions of not only the electronic structures [13,21,64], but also structural and thermodynamical properties of both β and λ phases (See Supplementary Note 1 for more detailed discussions). The D3 dispersion corrections [65] were not included, since for strongly ionic bulk materials the D3 corrections are not expected to be accurate and we found that inclusion of D3 correction deteriorates the description of lattice parameters and energy differences between the two phases (See Supplementary Table 1). The harmonic phonon dispersions were calculated by finite displacements using the Phonopy code [66]. The anharmonic phonon dispersions at finite temperatures were obtained using the temperature-dependent effective potential method [67] and the anharmonic force constants were extracted using the ALAM-ODE code [68]. The variable-cell climbing image nudged elastic band method [69] was used to estimate the energy barrier for the β - λ phase transition.

Machine learning potential construction and validation

The training dataset was initially constructed using the on-the-fly active learning method based on the Bayesian linear regression [70,71] using the separable descriptors [72], which allows us to efficiently sample the phase space and automatically collect the representative training structures during the AIMD simulations. The cutoff radius for the three-body descriptors and the width of the Gaussian functions used for broadening the atomic distributions of the three-body descriptors were set to 6 Å and 0.4 Å, respectively. The number of radial basis functions and maximum three-body momentum quantum number of the spherical harmonics used to expand the atomic distribution for the three-body descriptors were set to 14 and 4, respectively. The parameters for the two-body descriptors were the same as those for the three-body descriptors. The AIMD simulations were performed by heating the β - and λ -Ti₃O₅ phases of 96-atom supercell from 100 to 1500 K at ambient pressure and 10 GPa, in an isothermal-isobaric ensemble using a Langevin thermostat [73] combined with the Parrinello-Rahman method [74,75]. Eventually, 3,277 structures were selected in this step.

Since the phase transition from β - to λ -Ti₃O₅ is a barrier-crossing process, unbiased MD simulations hardly sample the PES along the transition path, even using the MLP at high temperatures. To address this issue, we first refitted the on-the-fly generated dataset using a moment tensor potential (MTP) [50] that is in general one order of magnitude faster than the kernel-based methods for a comparable accuracy [76,77]. For the MTP potential training, a cutoff radius of 6.0 Å was used, and the radial basis size was set to be 8. The MTP basis functions were selected such that the level of scalar basis B_α is less than or equal to 26 (i.e., $\text{lev}B_\alpha \leq 26$). The weights expressing the importance of energies, forces, and stress tensors were set to be 1.0, 0.05, and 0.05, respectively. The regression coefficients (in total, 2,153) were obtained by a non-linear least square optimization using the Broyden-Fletcher-Goldfarb-Shanno algorithm [78]. Employing the generated MTP, we performed a long-timescale metadynamics simulations at 600 K and 0 GPa on a 96-atom supercell using the intensity of the XRD peak at $2\theta = 22^\circ$ as a collective variable following ref. [46] (see Fig. 1a). Afterwards, we computed the extrapolation grade for the structures from the metadynamics trajectory according to the D-optimality criterion [79]. The structures with the extrapolation grade over 3.0 (in total, 498 structures) were selected and added to the on-the-fly generated dataset. In the end, the training dataset contained 3,775 structures of 96 atoms, on which the final MTP potential was trained using the MLIP package [80].

The MTP potential was validated on a test dataset containing 748

structures of 96 atoms, which were randomly chosen from a metadynamics trajectory at 600 K using the generated MTP potential. These test structures cover a fraction of the phase space represented by the training dataset, as illustrated by the kernel principal component analysis in Supplementary Fig. 2a. The training and validation root-mean-square-errors (RMSEs) on energies, forces, and stress tensors calculated by the MTP are illustrated in Supplementary Fig. 2, showing a high accuracy of the generated MTP. Moreover, the accuracy of the MTP was carefully validated by predicting the lattice parameters, energy-volume curves, and phonon dispersion relations of both β - and λ -Ti₃O₅, exhibiting excellent agreement with the underlying PBE results as well as available experimental data (see Supplementary Fig. 1b-c and Supplementary Table 1).

Metadynamics simulations

In order to simulate the β - λ phase transition and calculate the thermodynamic phase diagram, metadynamics simulations at various temperatures and pressures were carried out using the WT-MetaD [42]. The isothermal-isobaric WTMetaD simulations were carried out using the LAMMPS code [81] patched with the PLUMED code [82]. The temperature was controlled using the stochastic velocity rescaling thermostat [83] with a relaxation time 0.1 ps. The pressure was controlled with the Parrinello-Rahman barostat [75] with a relaxation time of 10 ps. The equations of motion were integrated using a time step of 2 fs. The bias factor that characterizes the rate of change of the deposited Gaussian height was set to 20. Gaussians with a width of 1 CV unit and an initial height of 5 kJ/mol were deposited every 1 ps to construct the history-dependent bias potential. For the choice of collective variable, the intensity of the XRD peak at $2\theta = 22^\circ$ was used, following ref. [46] (Fig. 1a). The Gibbs free energies were computed using the reweighting technique [53].

For the description of layer-by-layer growth, we employed the summation of the projected displacements of all the Ti3-Ti3 dimers along the a and c axes in each layer as the CVs, which are able to describe the degree of rotations of Ti3-Ti3 dimers in each layer and well distinguish the four phases (i.e., β , $\beta\beta\lambda$, $\beta\lambda\lambda$ and λ) (see Supplementary Fig. 6a for details). When calculating the PES for a concerted β - λ phase transition in a three-layer structure, the two CVs of the second layer d_2 and the third layer d_3 were constrained to be equal to that of the first layer d_1 so that all the three layers were forced to transform simultaneously from β to λ . For the WTMetaD simulations, the width and the initial height of Gaussian were set to 1.2 Å and 25 kJ/mol, respectively. The bias factor was set to 30. The time interval for the deposit of Gaussians was set to 0.5 ps. The simulation time was set as 200 ns to ensure the convergence. After the sampling was finished, we reweighted the data to obtain the desired free energy surface using an on-the-fly strategy [84].

Molecular dynamics simulations

MD simulations were performed using the LAMMPS code [81] in an isothermal-isobaric ensemble. The temperature was controlled using a Nosé-Hoover thermostat [85–87] with a relaxation time of 0.2 ps. The pressure was controlled with the Parrinello-Rahman barostat [75] with a relaxation time of 0.1 ps. For the c -axis unidirectional continuous tensile MD simulations, a supercell consisting of $12 \times 36 \times 12$ 32-atom conventional cells (in total 165,888 atoms) was used. The strain rate was set to be 10^8 /s. To model the intra-layer 2D growth behavior from β - to λ -Ti₃O₅, we built a β -Ti₃O₅ supercell consisting of $16 \times 48 \times 5$ 32-atom conventional cells (in total, 122,880 atoms) and then artificially created a λ -Ti₃O₅ layer (with a thickness equal to the c -axis lattice constant of 32-atom conventional cell) in a region with a radius of 60 Å in the middle of the supercell (see

Fig. 4a-b).

Data Availability

The data including the crystal structures and phonon dispersions of all predicted stable and metastable phases, training and validation datasets, and the developed machine learning potential have been deposited in the figshare repository (doi:10.6084/m9.figshare.24279616) (ref. [88]). The structure models used are provided in Supplementary Data. Source data are provided with this paper. The other data that support the findings of this study are available from the corresponding author upon request.

Code Availability

VASP can be acquired from the VASP Software GmbH (see www.vasp.at); MLIP is available at mlip.skoltech.ru; LAMMPS is available at www.lammps.org; PLUMED is available at www.plumed.org; OVITO is available at www.ovito.org; ALAMODE is available at alamode.readthedocs.io; Phonopy is available at phonopy.github.io/phonopy.

References

- [1] Porter, D. A., Easterling, K. E. & Sherif, M. Y. *Phase Transformations in Metals and Alloys (4th ed.)* (CRC Press, 2021).
- [2] Jr, C., D, W. & Rethwisch, D. G. *Fundamentals of materials science and engineering: an integrated approach* (John Wiley & Sons, 2020).
- [3] Grünebohm, A. *et al.* A unifying perspective of common motifs that occur across disparate classes of materials harboring displacive phase transitions. *Advanced Energy Materials* 2300754 (2023).
- [4] Irifune, T., Kurio, A., Sakamoto, S., Inoue, T. & Sumiya, H. Ultrahard polycrystalline diamond from graphite. *Nature* **421**, 599–600 (2003).
- [5] Luo, K. *et al.* Coherent interfaces govern direct transformation from graphite to diamond. *Nature* **607**, 486–491 (2022).
- [6] Kirby, S. H., Durham, W. B. & Stern, L. A. Mantle phase changes and deep-earthquake faulting in subducting lithosphere. *Science* **252**, 216–225 (1991).
- [7] Cheng, B., Hamel, S. & Bethkenhagen, M. Thermodynamics of diamond formation from hydrocarbon mixtures in planets. *Nature Communications* **14**, 1104 (2023).
- [8] Tolédano, P. & Dmitriev, V. *Reconstructive Phase Transitions: In Crystals and Quasicrystals* (WORLD SCIENTIFIC, 1996).
- [9] Zhu, S., Yan, X., Liu, J., Oganov, A. R. & Zhu, Q. A revisited mechanism of the graphite-to-diamond transition at high temperature. *Matter* **3**, 864–878 (2020).
- [10] Tong, Q. *et al.* Machine learning metadynamics simulation of reconstructive phase transition. *Physical Review B* **103**, 054107 (2021).
- [11] Badin, M. & Martoňák, R. Nucleating a different coordination in a crystal under pressure: a study of the B1–B2 transition in NaCl by metadynamics. *Physical Review Letters* **127**, 105701 (2021).
- [12] Santos-Florez, P. A., Yanxon, H., Kang, B., Yao, Y. & Zhu, Q. Size-dependent nucleation in crystal phase transition from machine learning metadynamics. *Physical Review Letters* **129**, 185701 (2022).
- [13] Ohkoshi, S.-i. *et al.* Synthesis of a metal oxide with a room-temperature photoreversible phase transition. *Nature Chemistry* **2**, 539–545 (2010).
- [14] Tokoro, H. *et al.* External stimulation-controllable heat-storage ceramics. *Nature Communications* **6**, 7037 (2015).
- [15] Ohkoshi, S.-i. *et al.* Low-pressure-responsive heat-storage ceramics for automobiles. *Scientific Reports* **9**, 13203 (2019).
- [16] Mariette, C. *et al.* Strain wave pathway to semiconductor-to-metal transition revealed by time-resolved X-ray powder diffraction. *Nature Communications* **12**, 1239 (2021).
- [17] Saiki, T. *et al.* Selection rule for the photoinduced phase transition dominated by anisotropy of strain in Ti₃O₅. *Physical Review B* **105**, 075134 (2022).
- [18] Sun, P. *et al.* Ti₃O₅ nanofilm on carbon nanotubes by pulse laser deposition: Enhanced electrochemical performance. *Applied Surface Science* **548**, 149269 (2021).
- [19] Nakamura, Y., Sakai, Y., Azuma, M. & ichi Ohkoshi, S. Long-term heat-storage ceramics absorbing thermal energy from hot water. *Science Advances* **6**, eaaz5264 (2020).
- [20] Ohkoshi, S.-i., Yoshikiyo, M., MacDougall, J., Ikeda, Y. & Tokoro, H. Long-term heat-storage materials based on λ -Ti₃O₅ for green transformation (GX). *Chem. Commun.* **59**, 7875–7886 (2023).
- [21] Yang, B. *et al.* Flatband λ -Ti₃O₅ towards extraordinary solar steam generation. *Nature* **622**, 499 (2023).
- [22] Zheng, L. The preparation and oxygen-sensing properties of α -Ti₃O₅ thin film. *Sensors and Actuators B: Chemical* **88**, 115–119 (2003).
- [23] Zhang, X. *et al.* Preparation and oxygen sensing properties of Ti₃O₅ submicron rods. *Micro and Nano Letters* **11**, 811–813 (2016).
- [24] Zhao, P.-f. *et al.* Progress in Ti₃O₅: synthesis, properties and applications. *Transactions of Nonferrous Metals Society of China* **31**, 3310–3327 (2021).
- [25] Fu, X. *et al.* Influences of hole/electron-lattice coupling on phase transition between λ -Ti₃O₅ and β -Ti₃O₅. *Journal of Physics: Condensed Matter* **32**, 46LT01 (2020).
- [26] Takeda, T. & Ohkoshi, S.-i. Prediction of a tensile force-induced structural phase transition from β -Ti₃O₅ to λ -Ti₃O₅ by molecular dynamic simulations. *European Journal of Inorganic Chemistry* **2022**, e202101037 (2022).
- [27] Jütten, S. & Bredow, T. Anisotropy of the pressure effect in the Ti₃O₅ phase transition process resolved by direction-dependent interface propagation. *The Journal of Physical Chemistry C* **127**, 20530–20538 (2023).
- [28] Jütten, S. & Bredow, T. Doping effect on the electronic structure and heat-storage properties of Ti₃O₅. *The Journal of Physical Chemistry C* **127**, 10445–10452 (2023).

- [29] Deringer, V. L. *et al.* Gaussian process regression for materials and molecules. *Chemical Reviews* **121**, 10073–10141 (2021).
- [30] Behler, J. Four generations of high-dimensional neural network potentials. *Chemical Reviews* **121**, 10037–10072 (2021).
- [31] Unke, O. T. *et al.* Machine learning force fields. *Chemical Reviews* **121**, 10142–10186 (2021).
- [32] Liu, P., Verdi, C., Karsai, F. & Kresse, G. α - β phase transition of zirconium predicted by on-the-fly machine-learned force field. *Physical Review Materials* **5**, 053804 (2021).
- [33] Verdi, C., Karsai, F., Liu, P., Jinnouchi, R. & Kresse, G. Thermal transport and phase transitions of zirconia by on-the-fly machine-learned interatomic potentials. *npj Computational Materials* **7**, 156 (2021).
- [34] Thompson, A., Swiler, L., Trott, C., Foiles, S. & Tucker, G. Spectral neighbor analysis method for automated generation of quantum-accurate interatomic potentials. *Journal of Computational Physics* **285**, 316–330 (2015).
- [35] Zhang, L., Wang, H., Car, R. & E, W. Phase diagram of a deep potential water model. *Phys. Rev. Lett.* **126**, 236001 (2021).
- [36] Wen, T., Zhang, L., Wang, H., E, W. & Srolovitz, D. J. Deep potentials for materials science. *Materials Futures* **1**, 022601 (2022).
- [37] Vandermause, J. *et al.* On-the-fly active learning of interpretable bayesian force fields for atomistic rare events. *npj Computational Materials* **6**, 20 (2020).
- [38] Batzner, S. *et al.* E(3)-equivariant graph neural networks for data-efficient and accurate interatomic potentials. *Nature Communications* **13**, 2453 (2022).
- [39] Drautz, R. Atomic cluster expansion for accurate and transferable interatomic potentials. *Phys. Rev. B* **99**, 014104 (2019).
- [40] Pozdnyakov, S., Oganov, A. R., Mazhnik, E., Mazitov, A. & Kruglov, I. Fast general two- and three-body interatomic potential. *Phys. Rev. B* **107**, 125160 (2023).
- [41] Laio, A. & Parrinello, M. Escaping free-energy minima. *Proceedings of the National Academy of Sciences* **99**, 12562–12566 (2002).
- [42] Barducci, A., Bussi, G. & Parrinello, M. Well-tempered metadynamics: a smoothly converging and tunable free-energy method. *Physical Review Letters* **100**, 020603 (2008).
- [43] Barducci, A., Bonomi, M. & Parrinello, M. Metadynamics. *WIREs Computational Molecular Science* **1**, 826–843 (2011).
- [44] Behler, J., Martoňák, R., Donadio, D. & Parrinello, M. Metadynamics simulations of the high-pressure phases of silicon employing a high-dimensional neural network potential. *Physical Review Letters* **100**, 185501 (2008).
- [45] Yao, Y., Klug, D. D., Sun, J. & Martoňák, R. Structural prediction and phase transformation mechanisms in calcium at high pressure. *Physical Review Letters* **103**, 055503 (2009).
- [46] Niu, H., Piaggi, P. M., Invernizzi, M. & Parrinello, M. Molecular dynamics simulations of liquid silica crystallization. *Proceedings of the National Academy of Sciences* **115**, 5348–5352 (2018).
- [47] Niu, H., Bonati, L., Piaggi, P. M. & Parrinello, M. Ab initio phase diagram and nucleation of gallium. *Nature Communications* **11**, 2654 (2020).
- [48] Gartner, T. E., Piaggi, P. M., Car, R., Panagiotopoulos, A. Z. & Debenedetti, P. G. Liquid-liquid transition in water from first principles. *Physical Review Letters* **129**, 255702 (2022).
- [49] Yang, M., Karmakar, T. & Parrinello, M. Liquid-liquid critical point in phosphorus. *Phys. Rev. Lett.* **127**, 080603 (2021).
- [50] Shapeev, A. V. Moment tensor potentials: a class of systematically improvable interatomic potentials. *Multiscale Modeling & Simulation* **14**, 1153–1173 (2016).
- [51] Cheng, B. *et al.* Mapping materials and molecules. *Accounts of Chemical Research* **53**, 1981–1991 (2020).
- [52] Bartók, A. P., Kondor, R. & Csányi, G. On representing chemical environments. *Physical Review B* **87**, 184115 (2013).
- [53] Bonomi, M., Barducci, A. & Parrinello, M. Reconstructing the equilibrium Boltzmann distribution from well-tempered metadynamics. *Journal of Computational Chemistry* **30**, 1615–1621 (2009).
- [54] Jütten, S. & Bredow, T. First-principles investigation of electronic properties and phase transition of Ti_3O_5 . *The Journal of Physical Chemistry C* **126**, 7809–7817 (2022).
- [55] Ostwald, W. Studien über die bildung und umwandlung fester körper. *Zeitschrift für physikalische Chemie* **22**, 289–330 (1897).
- [56] Peng, Y. *et al.* Two-step nucleation mechanism in solid–solid phase transitions. *Nature Materials* **14**, 101–108 (2015).
- [57] Tanaka, K. *et al.* Structural phase transition between γ - Ti_3O_5 and δ - Ti_3O_5 by breaking of a one-dimensionally conducting pathway. *Crystal Growth & Design* **15**, 653–657 (2015).
- [58] Kamioka, H. *et al.* Time-resolved imaging and spectroscopy for the photo-induced phase transition in Ti_4O_7 . *Journal of Photochemistry and Photobiology A: Chemistry* **311**, 154–159 (2015).
- [59] Wang, X. *et al.* Data-driven prediction of complex crystal structures of dense lithium. *Nature Communications* **14**, 2924 (2023).
- [60] Kresse, G. & Furthmüller, J. Efficient iterative schemes for ab initio total-energy calculations using a plane-wave basis set. *Physical Review B* **54**, 11169–11186 (1996).
- [61] Perdew, J. P., Burke, K. & Ernzerhof, M. Generalized gradient approximation made simple. *Physical Review Letters* **77**, 3865–3868 (1996).
- [62] Perdew, J. P. *et al.* Restoring the density-gradient expansion for exchange in solids and surfaces. *Physical Review Letters* **100**, 136406 (2008).
- [63] Sun, J., Ruzsinszky, A. & Perdew, J. P. Strongly constrained and appropriately normed semilocal density functional. *Physical Review Letters* **115**, 036402 (2015).
- [64] Kobayashi, K. *et al.* Electronic structure and correlation in β - Ti_3O_5 and λ - Ti_3O_5 studied by hard x-ray photoelectron spectroscopy. *Phys. Rev. B* **95**, 085133 (2017).

- [65] Grimme, S., Antony, J., Ehrlich, S. & Krieg, H. A consistent and accurate ab initio parametrization of density functional dispersion correction (DFT-D) for the 94 elements H-Pu. *The Journal of Chemical Physics* **132**, 154104 (2010).
- [66] Togo, A. & Tanaka, I. First principles phonon calculations in materials science. *Scripta Materialia* **108**, 1–5 (2015).
- [67] Hellman, O., Abrikosov, I. A. & Simak, S. I. Lattice dynamics of anharmonic solids from first principles. *Phys. Rev. B* **84**, 180301 (2011).
- [68] Tadano, T., Gohda, Y. & Tsuneyuki, S. Anharmonic force constants extracted from first-principles molecular dynamics: applications to heat transfer simulations. *Journal of Physics: Condensed Matter* **26**, 225402 (2014).
- [69] Sheppard, D., Xiao, P., Chemelewski, W., Johnson, D. D. & Henkelman, G. A generalized solid-state nudged elastic band method. *The Journal of Chemical Physics* **136**, 074103 (2012).
- [70] Jinnouchi, R., Lahnsteiner, J., Karsai, F., Kresse, G. & Bokdam, M. Phase transitions of hybrid perovskites simulated by machine-learning force fields trained on the fly with bayesian inference. *Physical Review Letters* **122**, 225701 (2019).
- [71] Jinnouchi, R., Karsai, F. & Kresse, G. On-the-fly machine learning force field generation: application to melting points. *Physical Review B* **100**, 014105 (2019).
- [72] Jinnouchi, R., Karsai, F., Verdi, C., Asahi, R. & Kresse, G. Descriptors representing two- and three-body atomic distributions and their effects on the accuracy of machine-learned interatomic potentials. *J. Chem. Phys.* **152**, 234102 (2020).
- [73] Allen, M. P. & Tildesley, D. J. *Computer simulation of liquids* (Oxford University Press, 2017).
- [74] Parrinello, M. & Rahman, A. Crystal structure and pair potentials: a molecular-dynamics study. *Physical Review Letters* **45**, 1196–1199 (1980).
- [75] Parrinello, M. & Rahman, A. Polymorphic transitions in single crystals: a new molecular dynamics method. *Journal of Applied Physics* **52**, 7182–7190 (1981).
- [76] Zuo, Y. *et al.* Performance and cost assessment of machine learning interatomic potentials. *The Journal of Physical Chemistry A* **124**, 731–745 (2020).
- [77] Liu, P. *et al.* Combining machine learning and many-body calculations: coverage-dependent adsorption of CO on Rh(111). *Physical Review Letters* **130**, 078001 (2023).
- [78] Liu, D. C. & Nocedal, J. On the limited memory BFGS method for large scale optimization. *Mathematical Programming* **45**, 503–528 (1989).
- [79] Podryabinkin, E. V. & Shapeev, A. V. Active learning of linearly parametrized interatomic potentials. *Computational Materials Science* **140**, 171–180 (2017).
- [80] Novikov, I. S., Gubaev, K., Podryabinkin, E. V. & Shapeev, A. V. The MLIP package: moment tensor potentials with MPI and active learning. *Machine Learning: Science and Technology* **2**, 025002 (2021).
- [81] Thompson, A. P. *et al.* LAMMPS—a flexible simulation tool for particle-based materials modeling at the atomic, meso, and continuum scales. *Computer Physics Communications* **271**, 108171 (2022).
- [82] Tribello, G. A., Bonomi, M., Branduardi, D., Camilloni, C. & Bussi, G. Plumed 2: new feathers for an old bird. *Computer Physics Communications* **185**, 604–613 (2014).
- [83] Bussi, G., Donadio, D. & Parrinello, M. Canonical sampling through velocity rescaling. *The Journal of Chemical Physics* **126**, 014101 (2007).
- [84] Bussi, G. & Laio, A. Using metadynamics to explore complex free-energy landscapes. *Nature Reviews Physics* **2**, 200–212 (2020).
- [85] Nosé, S. A unified formulation of the constant temperature molecular dynamics methods. *The Journal of Chemical Physics* **81**, 511–519 (1984).
- [86] Hoover, W. G. Canonical dynamics: equilibrium phase-space distributions. *Physical Review A* **31**, 1695–1697 (1985).
- [87] Shuichi, N. Constant temperature molecular dynamics methods. *Progress of Theoretical Physics Supplement* **103**, 1–46 (1991).
- [88] Liu, M. *et al.* Layer-by-layer phase transformation in Ti₃O₅ revealed by machine learning molecular dynamics simulations. *figshare repository*. doi:10.6084/m9.figshare.24279616 (2024).

Acknowledgements

The work at the Institute of Metal Research is supported by the National Natural Science Foundation of China (Grant No. 52201030 and Grant No. 52188101), the National Key R&D Program of China 2021YFB3501503, Chinese Academy of Sciences (Grant No. ZDRW-CN-2021-2-5), and the National Science Fund for Distinguished Young Scholars (Grant No. 51725103). The work at the Northeastern University is supported by the National Natural Science Foundation of China (Grant No. 52331001). J.H. and H.N. acknowledge the supports from the National Natural Science Foundation of China (Grant No. 22003050) and the Research Fund of the State Key Laboratory of Solidification Processing (NPU), China (grant No. 2020-QZ-03). G.K. acknowledges the support from the Austrian Science Fund (FWF) within the SFB TACO (Project No. F 81-N).

Author Contributions

P.L. conceived the project. P.L. designed the research with the help of H.N., X.-Q.C. and L.Z.. M.L., J.W., P.L., J.H. and H.N. performed the calculations. X.-Q.C., G.K. and L.Z. supervised the project. X.Y., J.L., H.Y., B.Y., Y.S. and C.C. participated in discussions. P.L. wrote the manuscript with inputs from other authors. All authors comments on the manuscript. M.L., J.W. and J.H. contributed equally to this work.

Competing Interests

The authors declare no competing interests.

Supplementary Information to "Layer-by-layer phase transformation in Ti_3O_5 revealed by machine learning molecular dynamics simulations"

Mingfeng Liu,^{1,2,*} Jiantao Wang,^{1,2,*} Junwei Hu,^{3,*} Peitao Liu,^{1,†} Haiyang Niu,^{3,†} Xuexi Yan,¹ Jiangxu Li,¹
Haile Yan,⁴ Bo Yang,⁴ Yan Sun,¹ Chunlin Chen,¹ Georg Kresse,⁵ Liang Zuo,⁴, and Xing-Qiu Chen¹

¹ Shenyang National Laboratory for Materials Sciences, Institute of Metal Research, Chinese Academy of Sciences, Shenyang 110016, China

² School of Materials Science and Engineering, University of Science and Technology of China, Shenyang 110016, China

³ State Key Laboratory of Solidification Processing, International Center for Materials Discovery, School of Materials Science and Engineering,
Northwestern Polytechnical University, Xi'an 710072, China

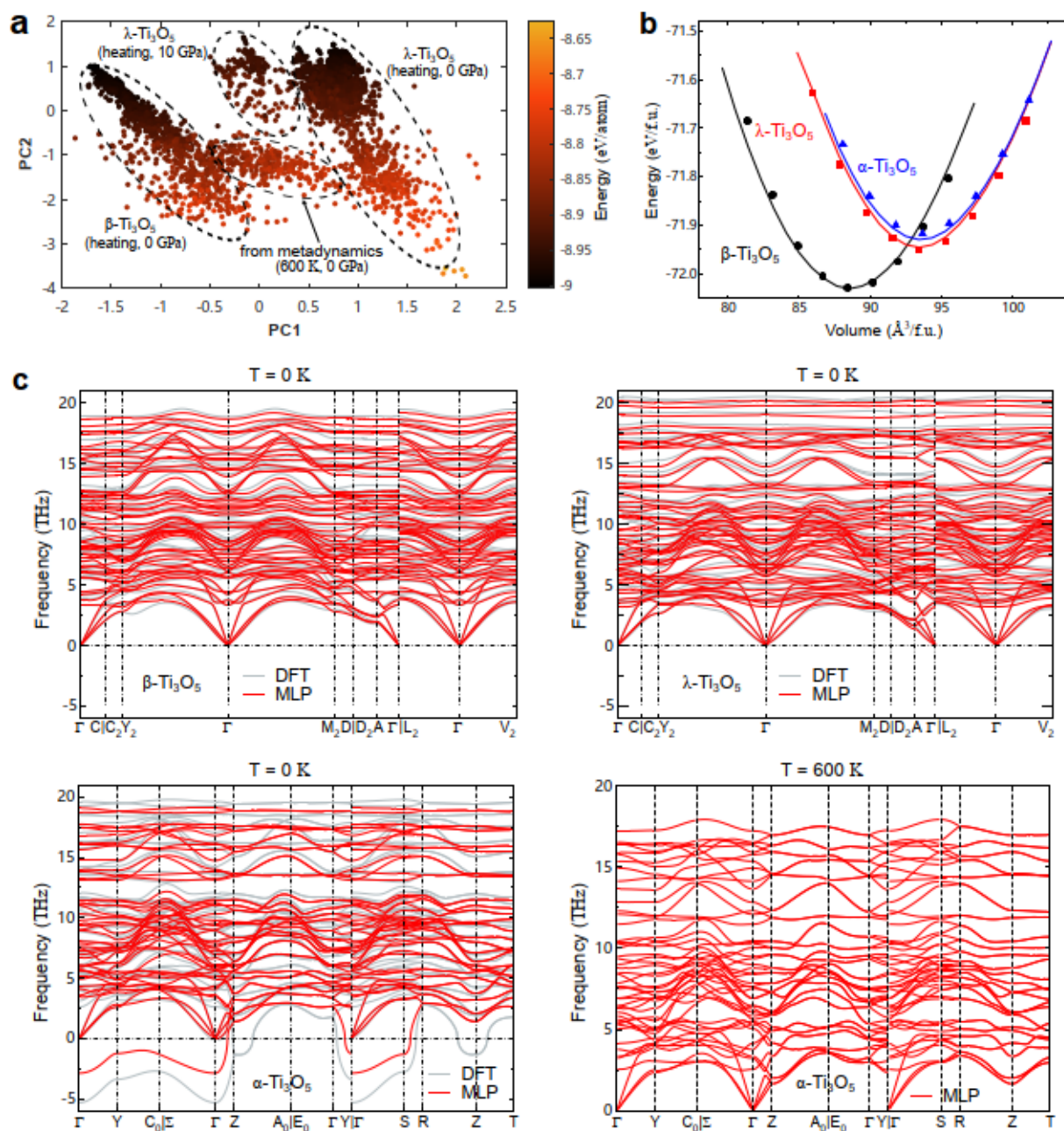
⁴ Key Laboratory for Anisotropy and Texture of Materials (Ministry of Education), School of Materials Science and Engineering, Northeastern
University, Shenyang 110819, China

⁵ University of Vienna, Faculty of Physics, Computational Materials Physics, Kolingasse 14-16, 1090 Vienna, Austria

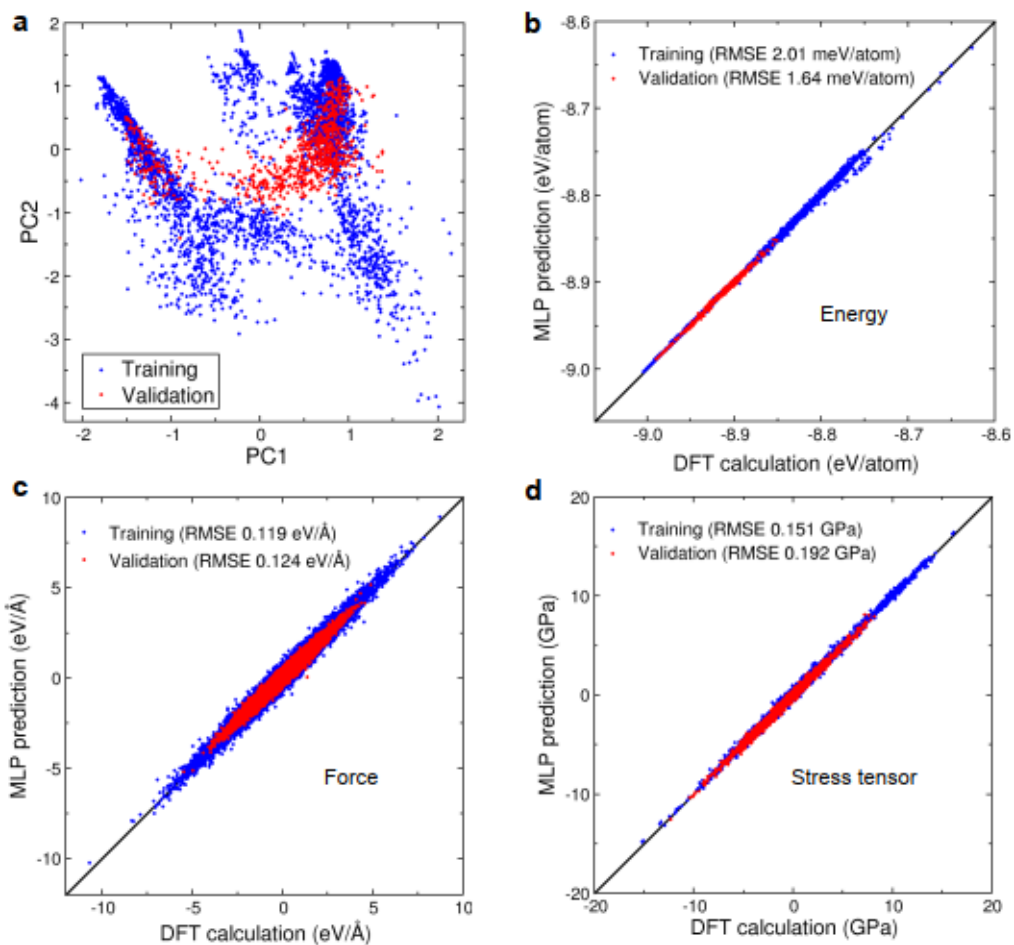
† Corresponding to: ptliu@imr.ac.cn, haiyang.niu@nwpu.edu.cn

* These authors contribute equally.

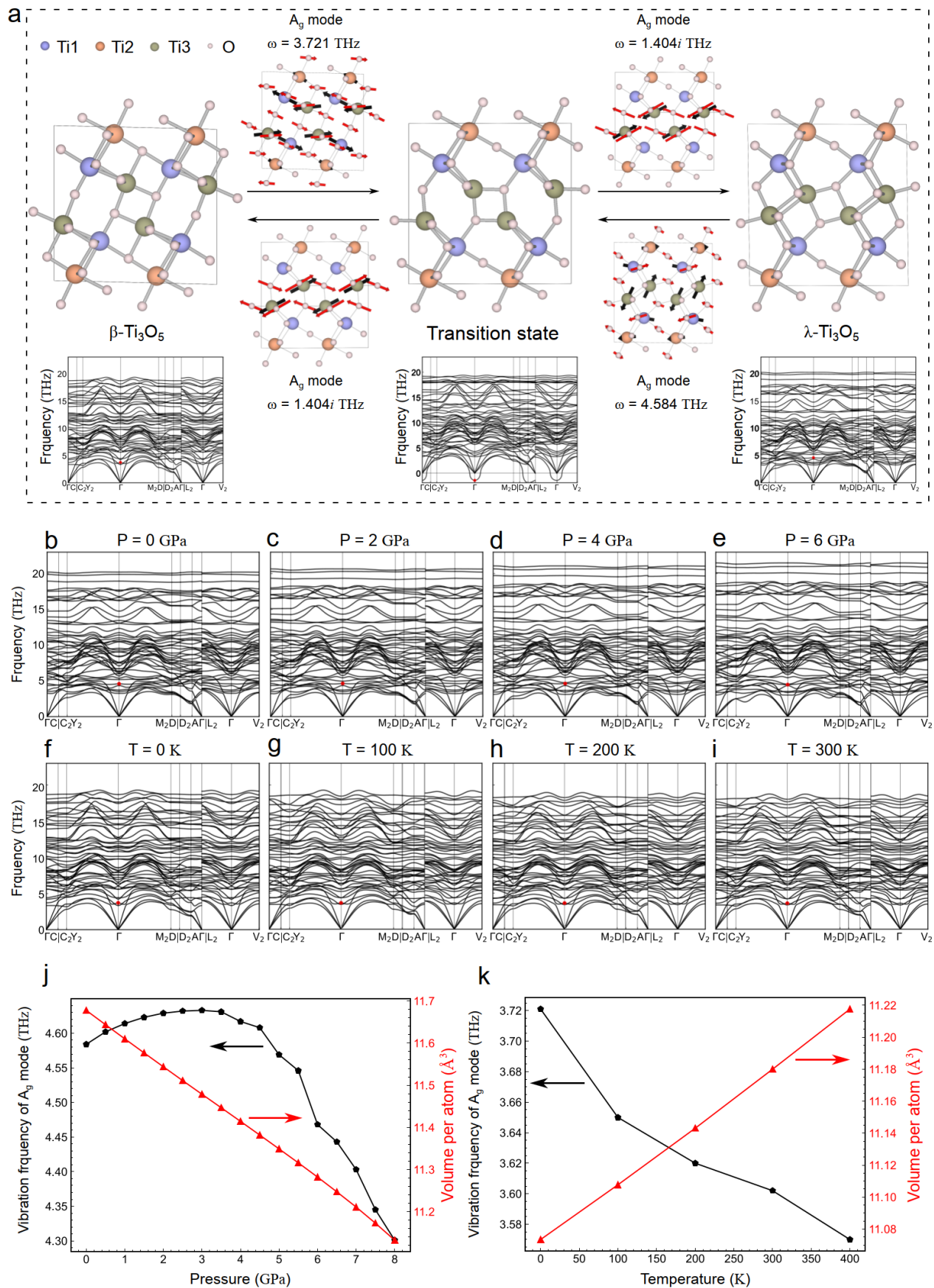
Supplementary Figures



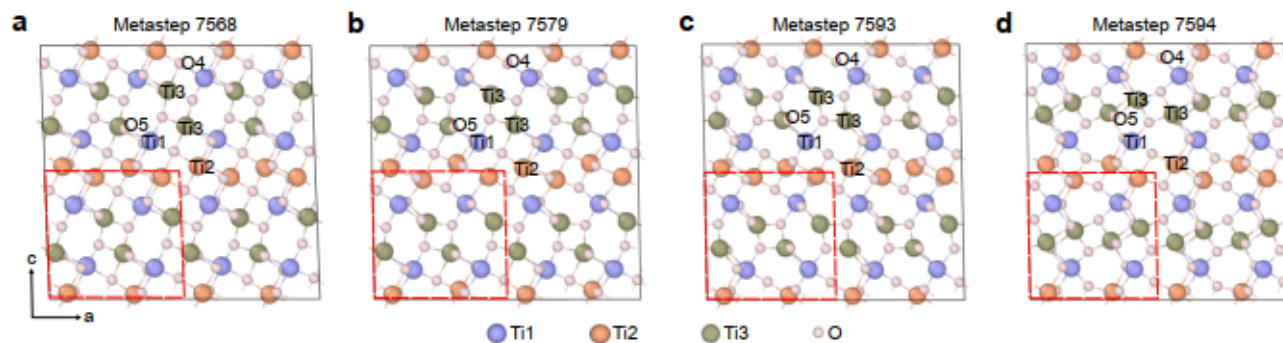
Supplementary Fig. 1. Machine learning potential (MLP) training and validation. **a**, The kernel principal component analysis map of the entire training structures. The map is color-coded according to the energy per atom. **b**, Energy-volume curves predicted by DFT (circles and squares) and MLP (solid lines). The energy is given in electron volt per formula unit (eV/f.u.). **c**, Phonon dispersion relationships predicted by DFT (gray lines) and MLP (red lines).



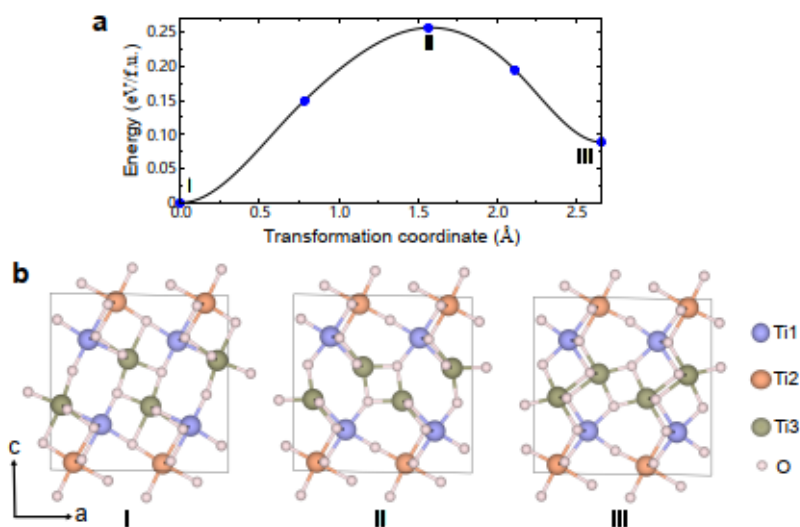
Supplementary Fig. 2. Training and validation datasets and machine learning potential (MLP) predictions vs. DFT results. a, The kernel principal component analysis map of training structures (blue squares) and validation structures (red squares). b, MLP predicted energies vs. DFT results. c, MLP predicted forces vs. DFT results. d, MLP predicted stress tensors vs. DFT results.



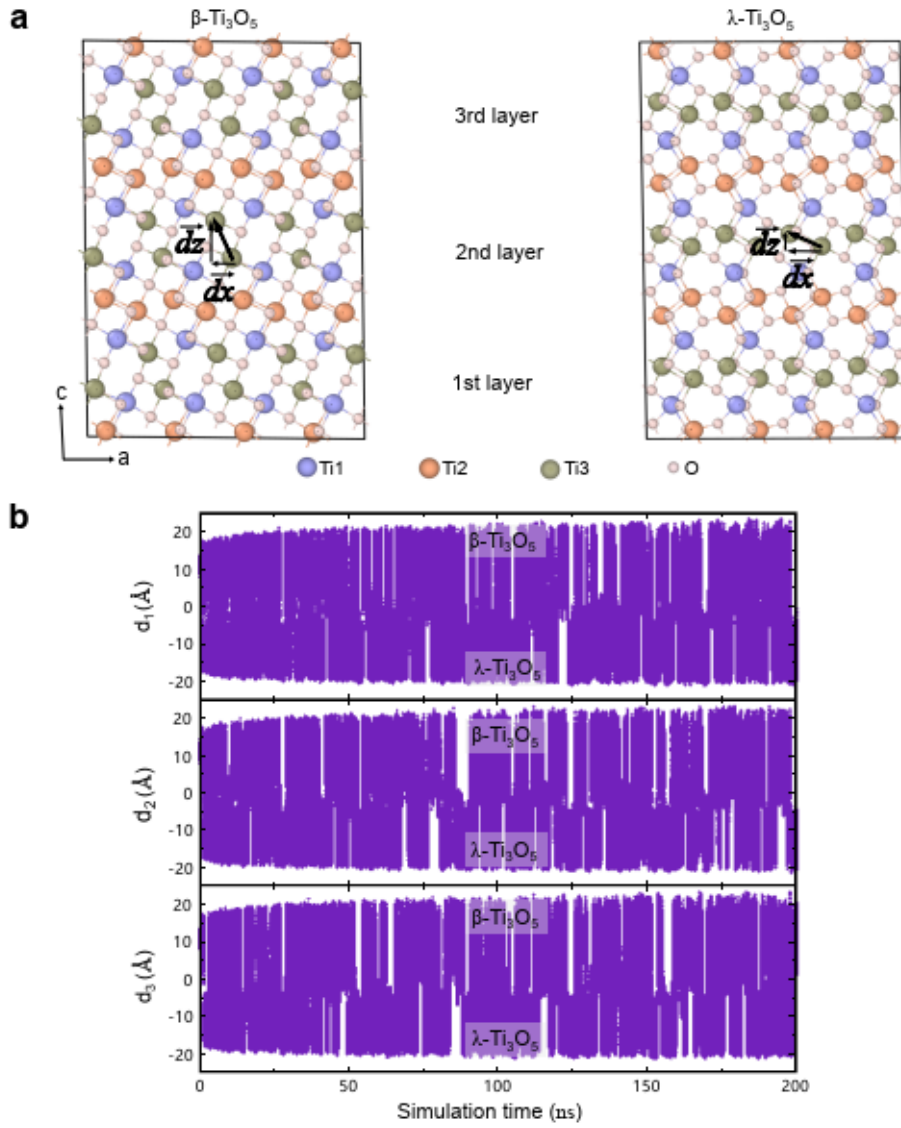
Supplementary Fig. 3. Phonon mode analysis. **a**, The decisive phonon modes that drive the phase transformation from β to λ , and vice versa. The arrows on the atoms indicate the atomic displacements associated with the specified phonon mode. **b-e**, Pressure-dependent phonon dispersions of λ - Ti_3O_5 . **f-i**, Temperature-dependent phonon dispersions of β - Ti_3O_5 . **j**, Pressure-dependent A_g phonon mode frequencies and system volumes of λ - Ti_3O_5 . **k**, Temperature-dependent A_g phonon mode frequencies and system volumes of β - Ti_3O_5 . Note that the red dots in the plots of phonon dispersions indicate the A_g phonon mode.



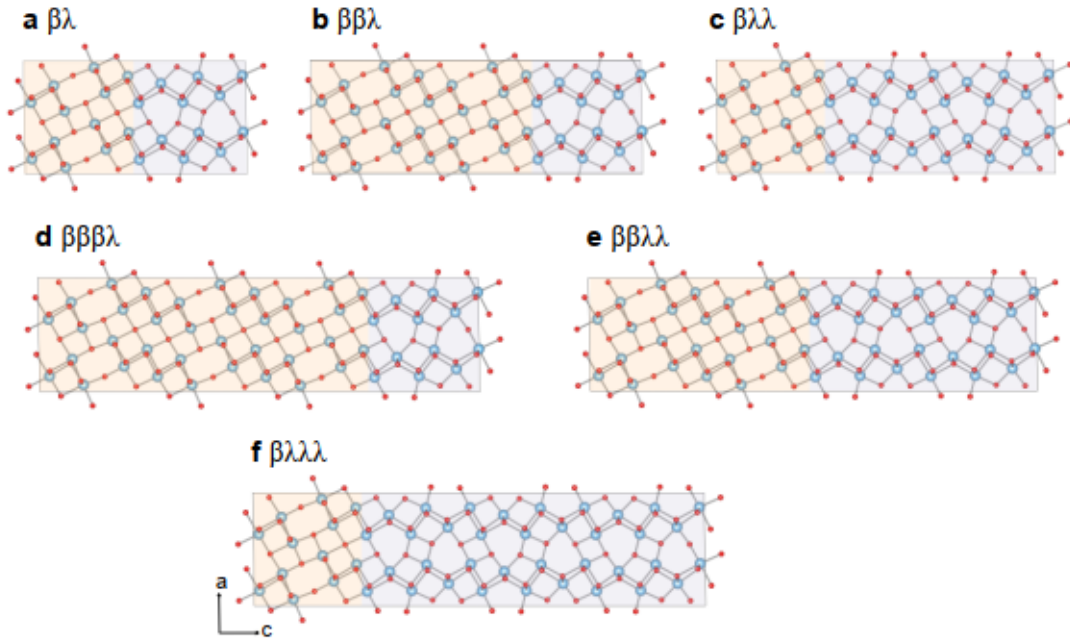
Supplementary Fig. 4. Snapshots extracted from a metadynamics simulation at 500 K. **a**, Snapshot extracted at metastep 7568. **b**, Snapshot extracted at metastep 7579. **c**, Snapshot extracted at metastep 7593. **d**, Snapshot extracted at metastep 7594. For a better visualization, here the employed supercell (indicated by red dashed lines) is doubled along both the a and c directions.



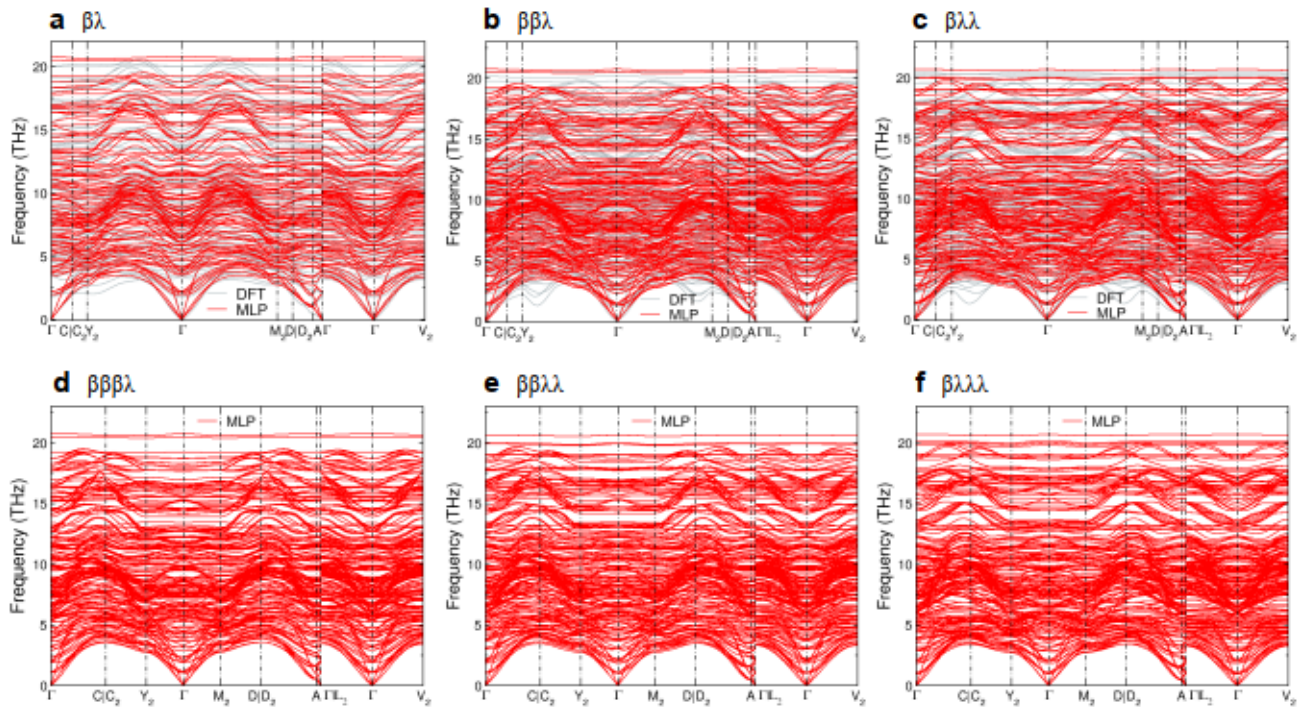
Supplementary Fig. 5. Variable-cell climbing image nudged elastic band calculations using DFT. **a**, The relative energy as a function of transformation coordinate. The energy is given in electron volt per formula unit (eV/f.u.). The calculated data are represented by blue circles, while the black curve corresponds to the spline fit. **b**, The structures of initial (I, corresponding to β), transitional (II), and final (III, corresponding to λ) phases.



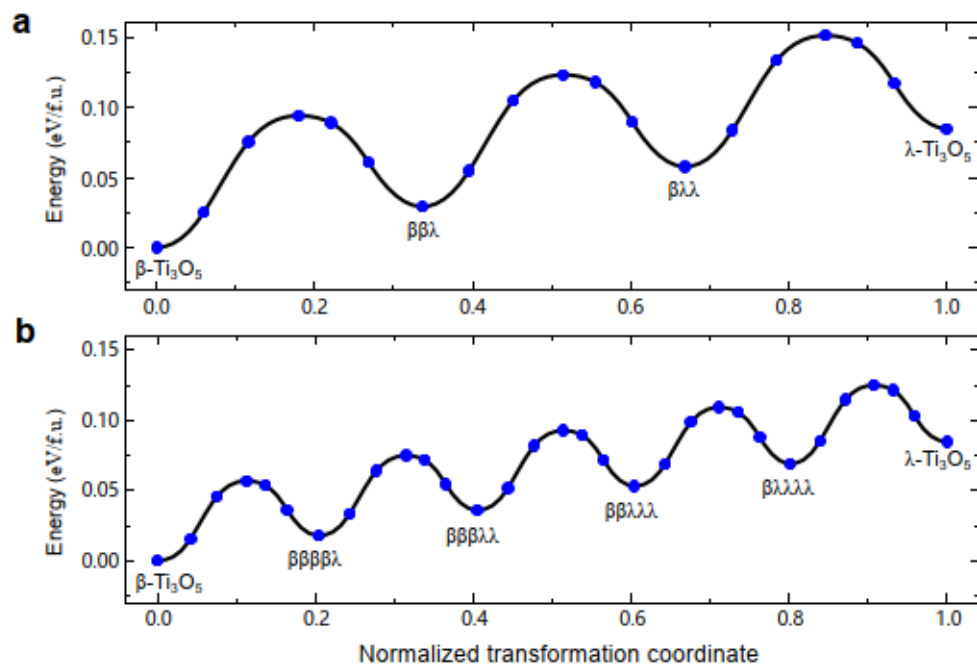
Supplementary Fig. 6. Collective variables design and their time evolution. **a**, The collective variable employed for describing the layer-by-layer growth in a three-layer structure are defined as $d_1 = \sum_{i \in 1\text{st Ti3-Ti3 layer}} ([\vec{d}_x]^i + [\vec{d}_z]^i)$, $d_2 = \sum_{i \in 2\text{nd Ti3-Ti3 layer}} ([\vec{d}_x]^i + [\vec{d}_z]^i)$, and $d_3 = \sum_{i \in 3\text{rd Ti3-Ti3 layer}} ([\vec{d}_x]^i + [\vec{d}_z]^i)$. Here, $[\vec{d}_x]^i$ and $[\vec{d}_z]^i$ represent the projected displacements of the i -th Ti3-Ti3 dimer in a layer along the a and c axes, respectively. **b**, The collective variables as a function of simulation time. The metadynamics simulations here were performed at 600 K and 0 GPa using a supercell of 384 atoms containing three Ti3-Ti3 layers along the c direction.



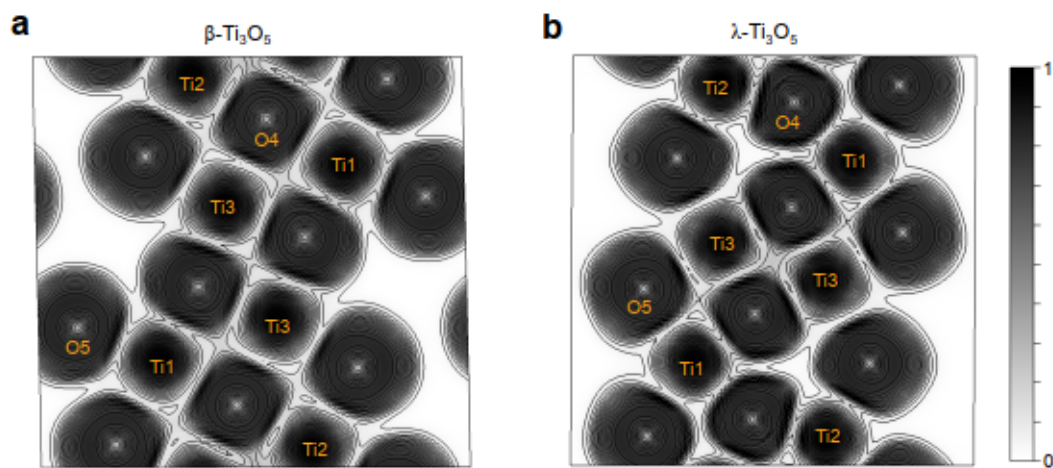
Supplementary Fig. 7. Predicted novel metastable phases. **a**, Structure of $\beta\lambda$ -stacking phase. **b**, Structure of $\beta\beta\lambda$ -stacking phase. **c**, Structure of $\beta\lambda\lambda$ -stacking phase. **d**, Structure of $\beta\beta\beta\lambda$ -stacking phase. **e**, Structure of $\beta\beta\lambda\lambda$ -stacking phase. **f**, Structure of $\beta\lambda\lambda\lambda$ -stacking phase. The light yellow and purple colors represent the β -like and λ -like local structural motifs, respectively. As an example, the notation of “ $\beta\beta\lambda$ ” indicates a metastable phase formed by sequentially stacking the β -like, β -like and λ -like local structural motifs along the c direction. We note that all structures with any combination of β -like and λ -like structural motifs along the c axis are dynamically stable, but here only the metastable phases with the number of stacking layers up to four are shown for brevity. The large blue and small red balls represent Ti and O atoms, respectively.



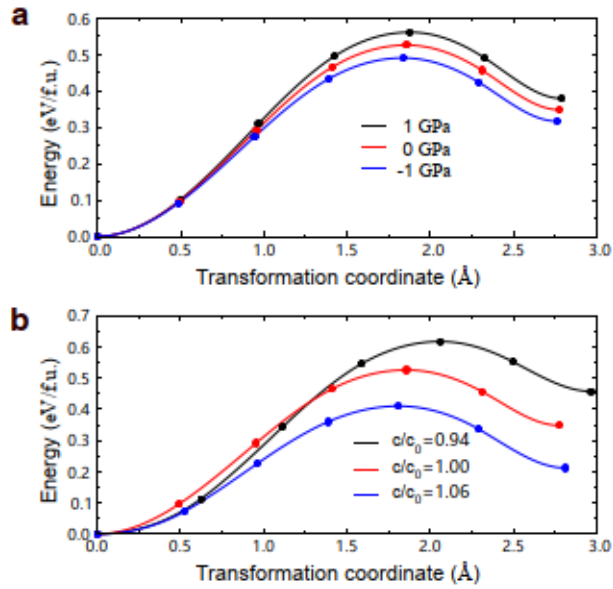
Supplementary Fig. 8. Machine learning potential (MLP) predicted phonon dispersion relationships for the metastable phases in Supplementary Fig. 7. **a**, Phonon dispersion of $\beta\lambda$ -stacking phase. **b**, Phonon dispersion of $\beta\beta\lambda$ -stacking phase. **c**, Phonon dispersion of $\beta\lambda\lambda$ -stacking phase. **d**, Phonon dispersion of $\beta\beta\beta\lambda$ -stacking phase. **e**, Phonon dispersion of $\beta\beta\lambda\lambda$ -stacking phase. **f**, Phonon dispersion of $\beta\lambda\lambda\lambda$ -stacking phase. For the phases ($\beta\lambda$, $\beta\beta\lambda$, and $\beta\lambda\lambda$) with small supercells, the DFT computed ones (in gray) are also shown for comparison.



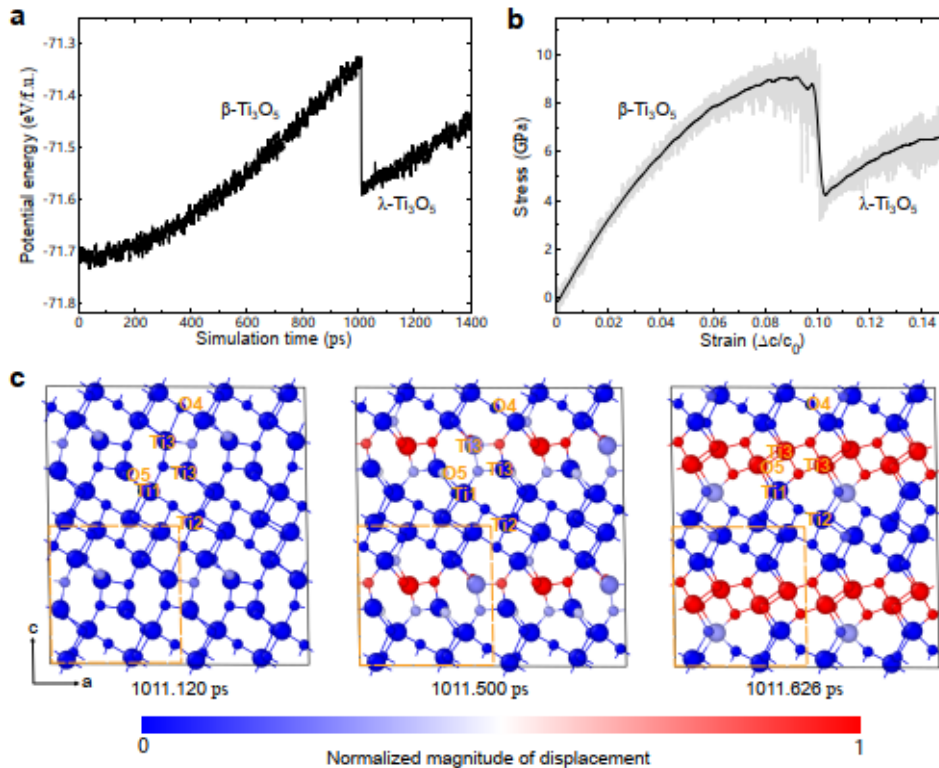
Supplementary Fig. 9. Variable-cell climbing image nudged elastic band calculations using machine learning potential. **a**, The relative energy as a function of normalized transformation coordinate for a three-layer-stacking supercell including 48 atoms. **b**, The relative energy as a function of normalized transformation coordinate for a five-layer-stacking supercell including 80 atoms. The energy is given in electron volt per formula unit (eV/f.u.).



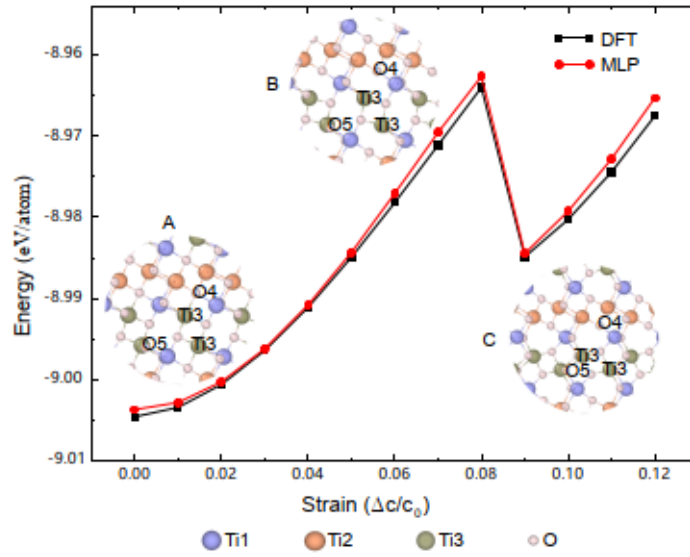
Supplementary Fig. 10. DFT calculated electron localization functions. **a**, β - Ti_3O_5 . **b**, λ - Ti_3O_5 . The relatively weak Ti3-O4 and Ti3-O5 chemical bonds can be identified for β - Ti_3O_5 and λ - Ti_3O_5 , respectively.



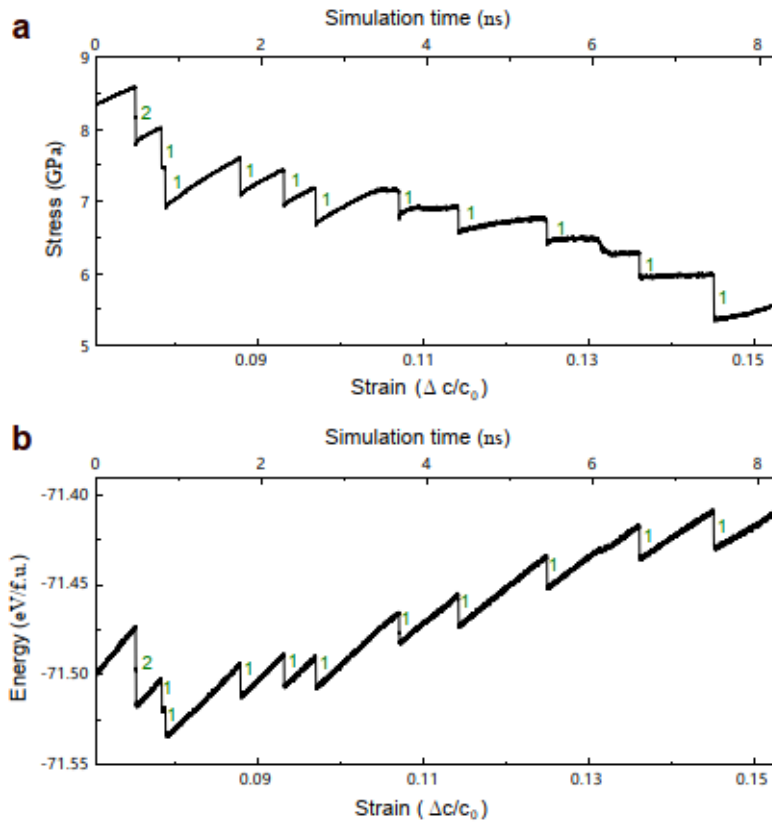
Supplementary Fig. 11. Pressure and strain dependence of energy barrier for the β to λ transition. a, Pressure dependence of energy barrier. b, c -axis unidirectional tensile strain dependence of energy barrier. Note that here the energy barriers were computed by fixed-cell climbing image nudged elastic band calculations using machine learning potential. The energy is given in electron volt per formula unit (eV/f.u.).



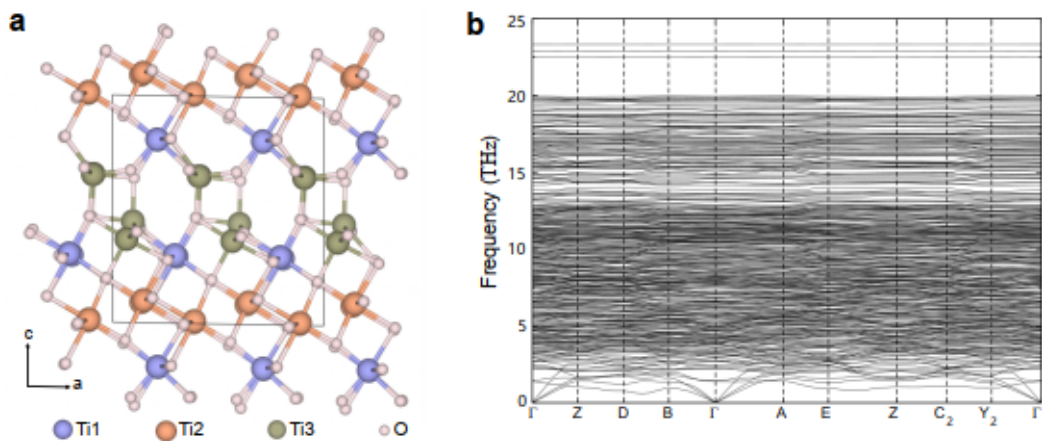
Supplementary Fig. 12. Direct molecular dynamics simulations under c -axis unidirectional continuous tensile strain (strain rate $10^8/s$) at 300 K and 0 GPa using a 96-atom cell. a, Evolution of potential energy with respect to simulation time. The energy is given in electron volt per formula unit (eV/f.u.). b, Stress-strain curve. c, Snapshots close to the phase transition. For a better visualization, here the employed supercell (indicated by yellow dashed lines) is doubled along both the a and c directions.



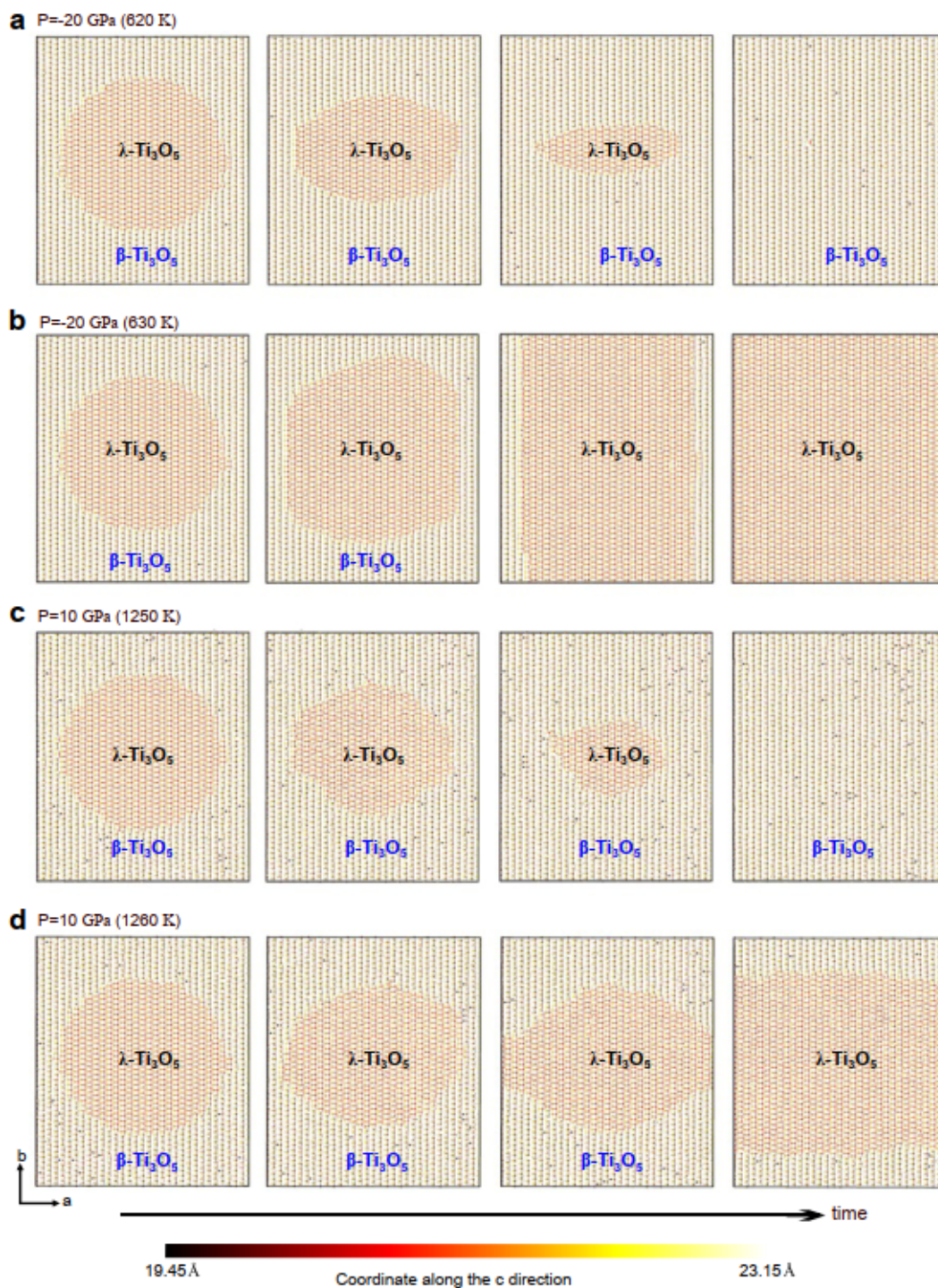
Supplementary Fig. 13. Total energies of a 32-atom cell predicted by DFT and machine learning potential (MLP) as a function of tensile strain along the c axis. The structures indicated by A, B, and C correspond to the strains ($\Delta c/c_0$) of 0.0, 0.08 and 0.09, respectively. c_0 is the c -axis lattice constant of β - Ti_3O_5 .



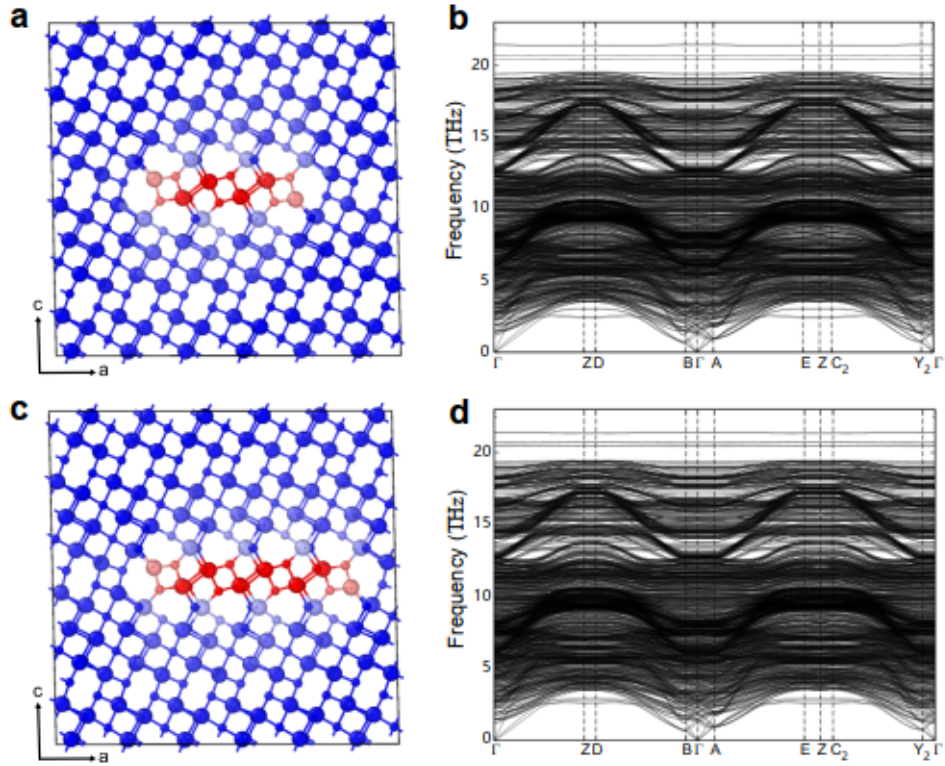
Supplementary Fig. 14. Evolution of the stress and potential energy of a large cell including 165,888 atoms with respect to strain under c -axis unidirectional continuous tensile strain. **a**, Evolution of stress. **b**, Evolution of potential energy. The employed strain rate here is $10^6/s$. The values close to each jump indicate the number of layers undergoing the β to λ transition. The energy is given in electron volt per formula unit (eV/f.u.).



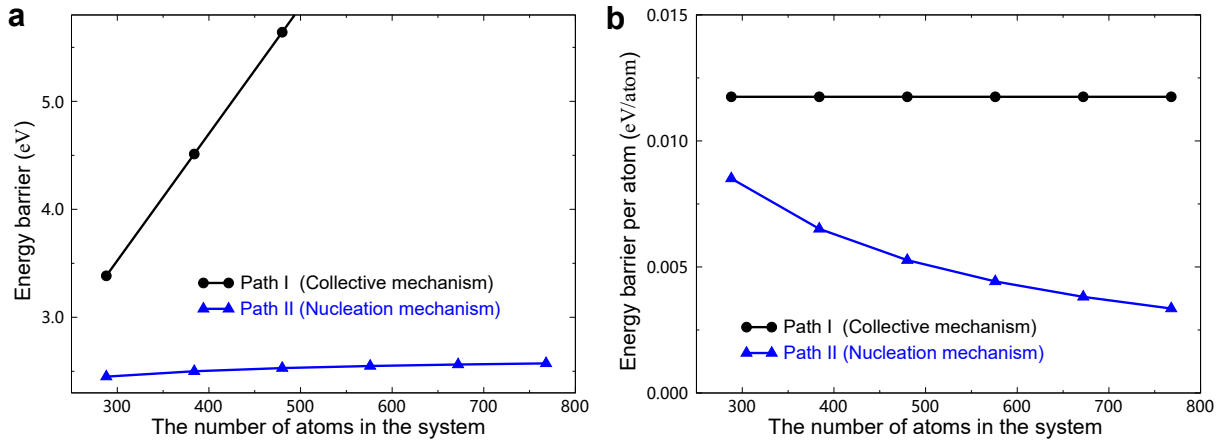
Supplementary Fig. 15. Defect-like metastable phase and its phonon dispersion. **a**, Crystal structure of the defect-like metastable phase. **b**, Phonon dispersion of the defect-like metastable phase. The metastable phase was obtained by elongating the c lattice constant in terms of the stable β - Ti_3O_5 phase and fully relaxing the other degree of freedoms. It will transform to the β phase after full structural relaxation (i.e., constraints are eliminated). The detailed structure information of this metastable phase is provided in Supplementary Data 1. The large and small balls in **a** represent the Ti and O atoms, respectively.



Supplementary Fig. 16. Large-scale in-plane phase growth molecular dynamics simulations at different temperatures and pressures. **a**, At the pressure of -20 GPa and the temperature of 620 K. **b**, At the pressure of -20 GPa and the temperature of 630 K. **c**, At the pressure of 10 GPa and the temperature of 1250 K. **d**, At the pressure of 10 GPa and the temperature of 1260 K.



Supplementary Fig. 17. Metastable phases observed during the in-plane growth process and their phonon dispersions. a-b Crystal structure of metastable phase B2 (Fig. 5 of the main text) and its phonon dispersion. c-d Crystal structure of metastable phase B4 (Fig. 5 of the main text) and its phonon dispersion. The large and small balls in a and c represent the Ti and O atoms, respectively.



Supplementary Fig. 18. System size dependence of energy barrier. a, Calculated energy barrier as a function of system size for two different phase transformation mechanisms from β to λ phases, i.e., collective mechanism (Path I) and nucleation mechanism (Path II). Note that for a better presentation the results for the case of the collective mechanism beyond the system size of 500 atoms are not shown. b, Calculated ratio between the energy barrier and the system size as a function of system size.

Supplementary Tables

Supplementary Table 1. The lattice parameters, volumes, energy differences between the two phases ΔE , phase transition temperature T_c , and phase transition enthalpy ΔH for a 32-atom unit cell predicted by PBE-derived machine learning potential (MLP), PBE, PBE+ U ($U=4.4$ eV), PBEsol, SCAN, and r²SCAN+D3. Note that nonmagnetic setups are adopted for all the methods except for PBE+ U and r²SCAN+D3 which consider the magnetic degrees of freedom. NM-M, AFM-I, FM-M, NM-S, and PM-M denote the nonmagnetic metal, antiferromagnetic insulator, ferromagnetic metal, nonmagnetic semiconductor, and paramagnetic metal, respectively. The energy is given in electron volt per formula unit (eV/f.u.).

	PBE-MLP	PBE	PBE+D3	PBE+ U	PBEsol	SCAN	r ² SCAN+D3	Experiments
β -Ti ₃ O ₅ ($C2/m$)	This work	This work	This work	This work	This work	This work	ref. [1]	ref. [2]
a (Å)	9.824	9.809	9.685	10.243	9.635	9.769	9.697	9.753
b (Å)	3.852	3.857	3.842	3.913	3.841	3.804	3.850	3.800
c (Å)	9.368	9.361	9.287	9.698	9.219	9.330	9.277	9.444
β (°)	91.333	91.204	91.024	92.321	91.089	91.355	91.068	91.532
Volume (Å ³)	354.35	354.10	345.50	388.35	341.09	346.66	346.30	349.90
Electronic state	—	NM-M	NM-M	AFM-I	NM-M	NM-M	FM-M	NM-S
λ -Ti ₃ O ₅ ($C2/m$)	This work	This work	This work	This work	This work	This work	ref. [1]	ref. [2]
a (Å)	9.840	9.851	9.699	10.114	9.568	9.655	9.808	9.831
b (Å)	3.795	3.787	3.801	3.881	3.815	3.799	3.808	3.788
c (Å)	10.007	10.023	9.908	10.320	9.809	9.928	9.930	9.970
β (°)	90.775	90.810	90.234	90.656	92.679	90.595	91.214	91.291
Volume (Å ³)	373.68	373.90	365.21	405.02	357.64	364.09	370.82	371.21
$\Delta E(\lambda - \beta)$ (eV/f.u.)	0.085	0.078	0.212	-0.175	0.174	0.163	0.110	—
$T_c(\lambda - \beta)$ (K)	535	—	—	—	—	—	525	470
$\Delta H(\lambda - \beta)$ (eV/f.u.)	0.091	—	—	—	—	—	0.098	0.124± 0.01
Electronic state	—	NM-M	NM-M	AFM-I	NM-M	NM-M	FM-M	PM-M
α -Ti ₃ O ₅ ($Cmcm$)	This work	This work	This work	This work	This work	This work	This work	ref. [3]
a (Å)	3.789	3.780	3.773	3.878	3.777	3.748	3.768	3.798
b (Å)	9.885	9.916	9.813	10.185	9.764	9.842	9.778	9.846
c (Å)	9.995	9.970	9.885	10.201	9.805	9.920	9.866	9.988
Volume (Å ³)	374.33	373.73	366.00	402.95	361.64	365.89	363.50	373.50
$\Delta E(\alpha - \beta)$ (eV/f.u.)	0.100	0.118	0.244	-0.301	0.239	0.216	0.258	—
Electronic state	—	NM-M	NM-M	AFM-I	NM-M	NM-M	NM-M	—

Supplementary Notes

Supplementary Note 1: The choice of the density functional

As mentioned in the main text, in this work the standard PBE functional with nonmagnetic setups were adopted for all the first-principle calculations. This is a very reasonable choice. The reasons are given as follows:

(i) The density functional theory calculations employing nonmagnetic setups yield good descriptions of the electronic structures of both β and λ phases, e.g., the formation of a bipolaron (with no spin) of Ti3-Ti3 caused by σ -type bonding of d_{xy} orbitals of Ti3 atoms in the β -Ti₃O₅ phase and the formation of slipped π -stacking between the d_{xy} orbital on Ti2 and the d_{xy} orbital on Ti3 in the λ -Ti₃O₅ phase [4–6].

(ii) The density functionals considering the magnetic setups often predict incorrect ground states that are not consistent with experiments. For instance, the hybrid functional M06-D3 predicts the β -Ti₃O₅ phase to be an antiferromagnetic (AFM) semiconductor, while predicts the λ -Ti₃O₅ phase to be a ferromagnetic (FM) semiconductor [1]. The r²SCAN-D3 method yields ferromagnetic metals for both β - and λ -Ti₃O₅ phases [1], while the PBE+*U* method predicts that the AFM order was found to be the ground states for both phases [7]. With *U*=4.4 eV the PBE+*U* method predicts an AFM insulator for all the three phases (β , λ , and α) and even yield qualitatively wrong negative values for the energy difference between the two phases (see Supplementary Table 1). We recall that in experiment the β phase is a nonmagnetic semiconductor, while the λ phase is a weak Pauli paramagnetic metal [4, 5].

(iii) The PBE functional with the nonmagnetic setups gives an excellent description of the experimental lattice parameters of β , λ as well as α phases as compared to other density functionals such as PBEsol and SCAN (see Supplementary Table 1).

(iv) Considering the magnetic degrees of freedom hardly changes the thermodynamical properties of both phases [1]. On the one hand, the calculated energy differences between different spin configurations are found to be small (see Table 1 of ref. [1]). On the other hand, the activation barriers from β to λ only change slightly between different magnetic configurations (see Table 3 of ref. [1]). We also compared the phase transition temperature T_c and phase transition enthalpy ΔH predicted by our PBE-derived machine learning potential (MLP) to the results predicted by r²SCAN+D3 as well as the experimental data. It can be seen from Supplementary Table 1 that the MLP fully accounting for the anharmonic phonon-phonon interactions yields a T_c of 535 K and ΔH of 0.091 eV/f.u., in good agreement with the predictions by the r²SCAN+D3 method within the simpler harmonic approximation (T_c =525 K and ΔH =0.098 eV/f.u.) [1]. Both are in line with the experimental results (T_c =460 K and ΔH =0.124±0.01 eV/f.u.) [2]. However, PBE is computationally cheaper and needs a fraction of the computational cost of the meta-GGA r²SCAN functional. Furthermore, including the magnetic degree of freedom will dramatically increase the complexity of MLP model. As far as we know, only few works currently attempt at incorporating the spin descriptor besides the structural descriptor into the MLP model.

Finally, we would like to briefly discuss the effect of the D3 dispersion correction on the structural and thermodynamical properties of β - and λ -Ti₃O₅. Generally, the D3 method is not accurate for ionic materials: in Ti₃O₅ charge is transferred from the Ti atoms to the oxygen atoms, but D3 and many other *posterior* corrections have not been designed to take this charge transfer into account. Furthermore, the D3 corrections have been parameterized to describe interactions through the vacuum, whereas in bulk materials the dispersion corrections are strongly screened by the surrounding atoms. The minimum level of complexity are thus many-body-dispersion corrections that account for the interplay between the polarizable entities. Hence, there is no reason to believe that D3 captures the relevant physics in Ti₃O₅. Indeed, we found that although both PBE and PBE+D3 give a correct positive energy difference between the two phases, PBE+D3 yields a significantly large value of 0.212 eV/f.u., far larger than the experimentally measured phase transition enthalpy (0.124±0.01 eV/f.u.) [2] (see Supplementary Table 1). In addition, we found that inclusion of the D3 correction slightly deteriorates the description of lattice parameters (see Supplementary Table 1). By contrast, the standard PBE functional yields excellent structural and thermodynamical properties of both phases. The predicted thermodynamical temperature-pressure phase diagram using the PBE-derived MLP is in good agreement with experiment (see Fig. 1 of the main text). We would like to stress that although the choice of the density functional would to some extent quantitatively change the actual values of the phase transition temperature and pressure, our main discovery of unusual layer-by-layer phase transformation initiated by kinetically favorable in-plane nucleated mechanism will remain unchanged by the change of the density functional.

Supplementary references

- [1] Jütten, S. & Bredow, T. First-principles investigation of electronic properties and phase transition of Ti₃O₅. *The Journal of Physical Chemistry C* **126**, 7809–7817 (2022).
- [2] Tokoro, H. *et al.* External stimulation-controllable heat-storage ceramics. *Nature Communications* **6**, 7037 (2015).
- [3] Onoda, M. Phase transitions of Ti₃O₅. *Journal of Solid State Chemistry* **136**, 67–73 (1998).
- [4] Ohkoshi, S.-i. *et al.* Synthesis of a metal oxide with a room-temperature photoreversible phase transition. *Nature Chemistry* **2**, 539–545 (2010).
- [5] Kobayashi, K. *et al.* Electronic structure and correlation in β -Ti₃O₅ and λ -Ti₃O₅ studied by hard x-ray photoelectron spectroscopy. *Phys. Rev. B* **95**, 085133 (2017).
- [6] Yang, B. *et al.* Flatband λ -Ti₃O₅ towards extraordinary solar steam generation. *Nature* **622**, 499 (2023).
- [7] Mariette, C. *et al.* Strain wave pathway to semiconductor-to-metal transition revealed by time-resolved X-ray powder diffraction. *Nature Communications* **12**, 1239 (2021).